Premixed hydrogen-methane combustion modelling with ECFM in a pre-chamber equipped RCEM

Fuel 415 (2026) 138455

Contents lists available at ScienceDirect

Fuel

journal homepage: www.elsevier.com/locate/fuel

Full Length Article

Premixed hydrogen-methane combustion modelling with ECFM in a pre-chamber equipped RCEM

Riccardo Sola [a,*], Mirko Baratta [a], Daniela Misul [a], Fabrizio Santonocito [a], Hiroshi Kawanabe [b]

[a] Politecnico di Torino, Corso Duca degli Abruzzi 24, Torino 10129, Italy
[b] Kyoto University, Yoshida-hommachi, Sakyo-ku, Kyoto 606-8501, Japan

ARTICLE INFO

Keywords:
Turbulent jet ignition
Combustion modelling
Hydrogen/methane mixture
Spark ignition
Combustion and flame characterization
Shadowgraph tecnique
High Karlovitz regime

ABSTRACT

Hydrogen is currently being investigated as an energy vector to decarbonize the transport sector, leveraging its numerous advantages as a fuel for internal combustion engines. This study builds on an experimental campaign aimed at assessing the impact of hydrogen enrichment in methane mixtures. Specifically, it evaluates the influence of hydrogen in a fully premixed, passive pre-chamber-equipped, spark-ignition Rapid Compression Expansion Machine (RCEM) under varying equivalence ratios and hydrogen contents. Additionally, the experimental dataset serves to validate the predictive capability of the flamelet-based Extended Coherent Flame Model (ECFM) in RANS numerical simulations.

Overall, the model demonstrates solid predictive capabilities, successfully capturing the experimental trends across all mixture compositions. In particular, it accurately predicts stoichiometric cases with hydrogen content ranging from pure hydrogen to a 25% volumetric ratio in methane. However, in lean cases ($\phi = 0.625$), the model exhibits greater discrepancies, requiring more extensive point-to-point calibration of the alpha stretch parameter. These discrepancies, along with the need for point-by-point calibration, are closely linked to the adaptability of the combustion model when the combustion regime is modified, due to variations in the chemical properties of the fuel blend. Furthermore, the pre-chamber system introduces different combustion processes as the flame is propagated from the pre-chamber to the main chamber, where combustion conditions differ significantly. The turbulence-chemistry interaction was analysed to link the calibration process to the combustion regime, using a detailed examination of the Borghi–Peters diagrams. Complementarily, two different kinetic mechanisms were employed to generate laminar flame speed values, enabling an assessment of the reliability of kinetic descriptions in parallel with turbulence–flame interaction modelling, thereby providing a more robust overall analysis.

1. Introduction

In recent years, it has become increasingly evident that addressing climate change requires the active involvement of all sectors and fields that significantly impact the environment. Decarbonizing the transport sector has emerged as one of the most widely discussed and debated topics in both academia and industry. This growing focus is driven by heightened concerns over greenhouse gas emissions, shifting attention from merely controlling pollutant emissions to reducing emissions that directly contribute to global warming. While fully electric vehicles play a crucial role, they cannot achieve alone the complete decarbonization of the transport sector. Consequently, research into decarbonizing internal combustion engines using zero-carbon fuels has gained increasing importance as a realistic pathway to reducing greenhouse gas emissions. Various projects focusing on new fuels generations are emerging, ranging from hydrogen to ammonia, also including biofuels and e-fuels, all aimed at reducing our reliance on fossil fuels.

Hydrogen is considered one of the most promising fuels for reducing fossil fuel dependence and greenhouse gas emissions, particularly when it is produced using renewable energy sources. Hydrogen is characterized by unique chemical and physical properties, which pose new and significant challenges when used as a fuel in conventional internal combustion engines. Its introduction redefines the concept of combustion, enabling lean and ultra-lean operation. Additionally, pre-chamber ignition presents a promising approach to expanding the engine's

* Corresponding author.
E-mail address: riccardo.sola@polito.it (R. Sola).

https://doi.org/10.1016/j.fuel.2026.138455
Received 14 April 2025; Received in revised form 2 January 2026; Accepted 17 January 2026
Available online 21 January 2026

Nomenclature

CoC	Centre of combustion
RCEM	Rapid compression expansion machine
ECFM	Extended coherent flame model
RANS	Reynolds-Averaged Navier-Stokes
TJI	Turbulent jet ignition
TCI	Turbulence-Chemistry interaction
LES	Large eddy simulation
DNS	Direct numerical simulation
ATDC	After top dead centre
AMR	Adaptive mesh refinement
ITNFS	Intermittent turbulent net flame stretch
LFS	Laminar flame speed
ISSIM	Imposed stretch spark ignition model
CAD	Crank angle degree
HR	Hydrogen ratio
ϕ	Equivalence ratio
α	Alpha stretch parameter
AHRR	Apparent heat release rate
CHR	Cumulative heat release
MFB	Mass fraction burnt
Da	Damköhler number
Ka	Karlovitz number

operational limits, allowing the use of extremely lean mixtures or low-reactivity fuels. Coupling these two concepts enables the design of an extremely efficient engine with near-zero carbon emissions and minimal NOx pollutants.

The pre-chamber as a combustion ignitor was extensively studied in the past and has recently regained attention due to the growing interest in lean combustion concepts aimed at reducing pollutant and carbon emissions [1–3]. From an experimental perspective, numerous studies have explored pre-chamber combustion systems to enhance combustion reactivity and enable lean and ultra-lean operations with various fuels, including hydrogen. Delving deeper into the topic of this paper, the growing interest in enhancing efficiency while reducing carbon emissions highlights the potential of hydrogen when coupled with other fuels. This approach is particularly appealing due to the storage challenges associated with hydrogen in passenger vehicles. Biswas et al. [4] provided a comprehensive analysis of pre-chamber combustion phenomena using methane and hydrogen, investigating the effects of key parameters such as spark location, orifice diameter, initial chamber pressure, and the influence of the equivalence ratio. They identified two distinct combustion regimes influenced by quenching phenomena occurring through the nozzle. Additionally, they highlighted the differences between hydrogen and methane combustion in a pre-chamber system, using optical diagnostic techniques to analyse flame propagation within the main chamber. Along similar lines, the same research group [5] investigated the flammability limits of pure hydrogen, determining the leanest mixture capable of ensuring ignition onset facilitated by a pre-chamber system. Gholamisheeri et al. [6] investigated the phenomenology of methane combustion using a turbulent jet ignition system in a rapid compression machine, examining the effects of varying orifice diameter and mixture equivalence ratio. Similarly, Rajasegar et al. [7] analysed the spatial and temporal progression of natural gas mixture combustion under lean-burn conditions, facilitated by a pre-chamber spark ignition system. Their study utilized optical diagnostic imaging and heat release analysis to gain deeper insights into the combustion process. Recent studies, such as the work by Pielecha et al. [8], have begun investigating methane-hydrogen blends to enhance the reactivity of pure methane mixtures, enabling lean and ultra-lean operating conditions through the use of a passive pre-chamber system. This approach makes the application of such technologies in modern internal combustion engines increasingly realistic. Their research also identified distinct combustion behaviours associated with varying hydrogen concentrations, focusing on the effects of spark advance while maintaining a consistent centre of combustion (CoC). On the other hand, Jin et al. [9] explored hydrogen enrichment in a conventional spark-ignition engine fuelled by methane, examining hydrogen concentrations ranging from 10% to 50% by volume. They tested different air–fuel ratios, spanning from slightly rich to lean mixtures. Despite the absence of a pre-chamber system, the addition of hydrogen ensured a reliable combustion process even under lean conditions, often requiring delayed ignition timing to fully capitalize on the benefits of hydrogen enrichment. Similarly, Soltic et al. [10] experimentally tested a spark-ignition engine equipped with a passive pre-chamber, comparing two mixtures: one with pure methane and another with a blend of methane and 22.5% hydrogen by volume. An important aspect of optimizing the design of a pre-chamber spark-ignition engine is determining the nozzle hole configuration, which has a significant impact on combustion and flame development. Jeelan Basha et al. [11] conducted an experimental campaign to evaluate the effects of varying hole configurations on the combustion of a methane-hydrogen mixture. Their findings demonstrated that the addition of hydrogen effectively extends the lean combustion limit, providing benefits across all aspects considered in the study.

The experimental data collected above are invaluable for both understanding the phenomena governing turbulent jet ignition and providing the necessary information to validate numerical models designed to predict this type of combustion process. From a numerical perspective, various studies have attempted to simulate the highly turbulent combustion process assisted by a pre-chamber system in spark-ignition engines, including cases with hydrogen addition to enhance fuel reactivity. Both approaches aim at increasing combustion intensity, enabling the use of lean and ultra-lean mixtures while avoiding misfires and minimizing cycle variability. In the context of internal combustion engines, the Reynolds-Averaged Navier-Stokes (RANS) turbulence model remains the most popular and effective approach due to its balance between computational efficiency and the ability to simulate complex combustion processes, such as those in TJI-equipped engines. Accordingly, several studies aim to simulate and predict the behaviour of pre-chamber combustion processes. On one hand, these studies demonstrate how combustion models and fine-tuning techniques can accurately predict and align with experimental data. On the other hand, once the simulation results are validated with sufficient experimental data, researchers leverage the numerical results to analyse the details of the TJI process or optimize the combustion system [12–17]. This optimization can involve modifying pre-chamber geometry or calibrating engine parameters that significantly impact performance. Most of the cited studies utilize detailed chemistry tools to model the combustion process, often coupled with one or multiple kinetic mechanisms, to bypass the calibration process and testing the predictive accuracy [18]. However, detailed chemistry models coupled with the RANS approach do not always perform effectively. For instance, Kim et al. [19] compared a sophisticated detailed chemistry model with commonly used flamelet models, such as the G-equation, and emphasized the critical role of turbulence-chemistry interaction (TCI) in the combustion process of TJI engines, particularly once the jets exit the nozzles. Uncertainties remain regarding the interaction between turbulence and flame propagation, particularly the effects of small- and large-scale eddies on flame thickness, sparking ongoing debates within the CFD community [20]. Detailed analyses of combustion regimes have proven valuable for understanding the limitations and applicability of various combustion models in internal combustion engines, demonstrating their

role as excellent test cases for advancing tools to effectively model complex phenomena [21,22]. Methodology as Piano et al. [23] proposed could particularly be useful to characterize the flame propagation phenomena enabling a better understanding how numerical model interact with the real phenomena that is modelling through the simulation, especially with a RANS (Reynolds-Averaged Navier-Stokes) approach. The paper also introduces an important aspect related to the influence of the pre-chamber system, demonstrating how the combustion processes occurring in the pre-chamber and main chamber can differ significantly. This differentiation enables the identification of different combustion regimes, which can be effectively analysed through the Borghi–Peters diagram. More sophisticated approach is used to better understand the flame turbulence interaction and the phenomenology of flame-wall interaction through the orifices that connect the pre-chamber and the main chamber. LES (Large Eddy Simulation) and DNS (Direct Numerical Simulation) approach tent to better represent these phenomena, clarifying the multiple processes that influence the rate of fuel consumption in the main chamber [24–26].

Given the challenges in numerical modelling in both the chemical composition of the fuel and the equivalence ratio of the mixture, this study aims at elucidating and clarifying the predictive capabilities of turbulence-combustion modelling applied to a passive pre-chamber engine fuelled by hydrogen/methane mixture. The study focuses on a perfectly homogeneous mixture and constant initial turbulence conditions to isolate the effects of chemistry-turbulence interaction. Various hydrogen/methane blends will be used to investigate the impact of hydrogen enrichment on a flamelet-based model under both stoichiometric and lean conditions, extending up to pure hydrogen operation. The wide range of operating conditions enables a comprehensive evaluation of the model's predictive capability by varying the combustion regime through changes in mixture properties and by comparing the combustion processes occurring in the pre-chamber and the main chamber. Since LES and DNS remain limited to niche applications due to their high computational cost, RANS is currently the most widely used approach for simulating turbulent combustion processes in engines, particularly from an industrial perspective. Aware of the critical role of TCI in pre-chamber combustion, particularly with new fuel types and mixtures, the ECFM (Extended Coherent Flame Model) was chosen to numerically analyse the influence of fuel chemistry in a passive pre-chamber engine. This choice was made despite the model's limitations in capturing quenching phenomena within the orifices [27]. Nevertheless, ECFM is well-suited for predicting turbulent premixed combustion in engine-like applications, as it incorporates a dedicated flame stretch model to account for the wrinkling effect of turbulence on the flame front [27,28]. Following the detailed description of the experimental apparatus and procedure in Section 2, and the computational setup for numerically predicting the combustion process in Section 3, this study first outlines the numerical procedure in Section 4. Subsequently, Section 5 emphasizes the correlation between experimental and numerical results, supported by optical imaging that captures flame propagation within the main chamber. Furthermore, this study aims to characterize turbulence-chemistry interaction and uncertainties in laminar flame speed, which represent key challenges in modelling premixed combustion for internal combustion engines. The experimental data were obtained at the Combustion and Power Engineering Laboratory, Graduate School of Energy Science, Department of Energy Conversion Science, Kyoto University. All numerical analyses were conducted by the PT-ERC Engine Research Group at the Polytechnic University of Turin.

2. Experimental data and engine description

2.1. Purpose

The experimental campaign aimed at investigating the hydrogen effect on the combustion process in a passive pre-chamber natural spark ignition engine. To better understand the influence of hydrogen, two different equivalence ratios were tested for each mixture: a stoichiometric condition and a leaner charge ($\phi = 0.625$). To achieve this, a rapid compression-expansion machine (RCEM) with optical access was used, allowing to capture images of the flame propagation. This optical access was combined with a shadowgraph technique, enabling identification of the flame front during the jet propagation process inside the main chamber.

2.2. Experimental apparatus and visualization device

The experimental apparatus was fabricated from a single-cylinder engine, which was modified to allow optical access using an extended piston. The apparatus also includes a premix tank, an ignition device, a control circuit, various sensors, and a data recording device. A schematic diagram of the entire system is shown in Fig. 1.

The RCEM used in this study is based on a horizontal, water-cooled, four-stroke, single-cylinder diesel engine (Yanmar NFD170) with a bore diameter of 102 mm and a stroke of 105 mm. A motor was connected to the flywheel, and the engine speed was controlled by an inverter, with the speed set to 900 rpm. The crank angle was measured every 0.5° CA using a rotary encoder attached to the crankshaft. Based on this crank angle data, the timing of the intake and exhaust valve openings and closings, as well as the ignition timing, were controlled by a custom-built timing controller. Additionally, the temperatures of the mixture in the premix tank and the outer wall of the premix tank were monitored. A synthetic quartz glass observation window is positioned between the upper part (piston extension top) and the lower part (piston extension body). In this experimental setup, methane, hydrogen, and compressed air are mixed inside the mixing tank before being drawn into the engine. In all cases, the pressure in the mixing tank was set to 1.4 bar, and the partial pressures were adjusted to create a mixture with the desired composition and equivalence ratio. The premixed fuel is generated by creating a low vacuum inside the cylinder and intake system using an oil rotary vacuum pump, which is branched off from the exhaust pipe. The valve, a pressure sensor for the main chamber, and a pre-chamber are positioned on the cylinder head. The bottom of the cylinder head was mirror-finished to facilitate shadowgraph photography. Fig. 2 shows a cross-sectional view of the pre-chamber with the main chamber which together form the combustion chamber. A pressure sensor was installed in the pre-chamber to measure the pre-chamber pressure. The pre-chamber was a passive type which did not use a fuel injection valve. Table 1 lists the geometry of the combustion chamber and the pre-

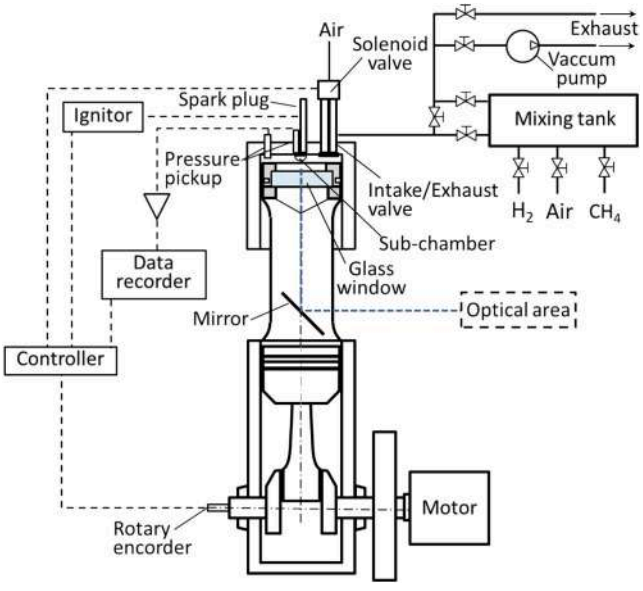

Fig. 1. Experimental apparatus scheme.

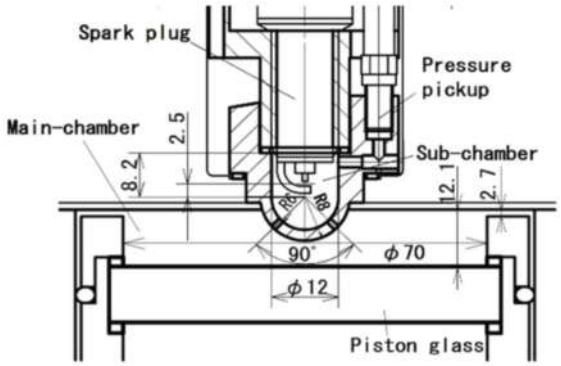

Fig. 2. Sectional view of the combustion chamber showing the main chamber and the pre-chamber with their respective dimensions listed in the table.

Table 1
Sectional view of the combustion chamber showing the main chamber and the pre-chamber with their respective dimensions listed in the table.

Engine Geometry	Values
Pre-chamber volume	1.47 cm3
Volume Ratio Pre/Main chamber	2.2%
Nozzles diameter	1.2 mm
Nozzles angle	90°
Piston window diameter	70 mm
Bowl depth	9.4 mm
Squish height	2.7 mm

chamber dimensions relative to the main chamber.

In this study, bottom-view shadowgraph photography with a high-speed camera were used to capture images of flame propagation, allowing visualization of the jet flame ejection behaviour and flame development. The shadowgraph method is well-suited for visualizing differences in refraction that occur when parallel light passes through a fluid with a density gradient, represented as variations in light and dark shading.

Fig. 3 shows a schematic diagram of the visualization setup. The resulting parallel light entered the cylinder head perpendicularly, directed by a mirror placed beneath the combustion chamber and reflected by the mirror-finished cylinder head. As shown in Fig. 2, the portion of the piston that allows light to pass through the glass and enter the main chamber is limited by the piston geometry and the dimensions of the glass insertion.

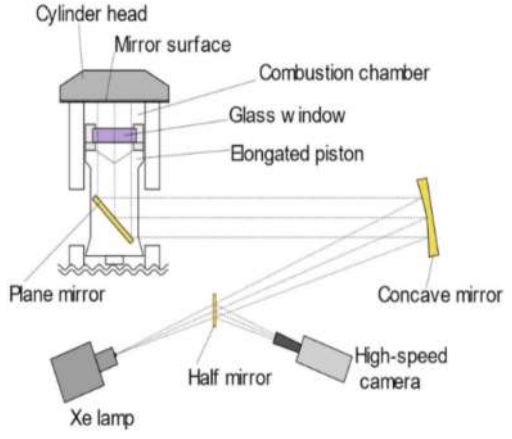

Fig. 3. Diagram of the visualization setup.

2.3. Experimental procedure

Before starting the procedure, the premix tank, intake pipe, and cylinder interior were placed under a low vacuum state lower than 0.3 kPa using a vacuum pump connected to the premix tank. Prior to this, the valve was closed, and the premix tank was filled with methane, hydrogen, and compressed air, adjusting the partial pressures to achieve the correct mixture composition. Immediately after activating the electric motor, the valve was opened to send the premixed mixture into the combustion chamber, creating a homogeneous charge after a certain number of motored cycles. A "Go" signal was sent once the valve temperature reached the target temperature (358 K), after which the valve received the closing signal, allowing the compression phase to begin. During the compression stroke, the ignition signal reached the spark plug, and combustion was recorded by the previously described system. Specifically, the ignition signal was output between −21° and −10.5° ATDC, with ignition confirmed at −10° ATDC. Immediately after combustion, the valve was opened to decrease the pressure inside the chamber, and then the motor was stopped. This procedure was repeated for each operating point tested, with a cool-down interval between tests to ensure nearly identical initial conditions.

Table 2 summarizes the main information about the setup used for the simulations. This experimental campaign focused on analysing the combustion process during flame development and propagation, providing the opportunity to quantify the influence of hydrogen using both signal and optical data. Optical images are available for a limited range of crank angles, enabling a focused analysis on the main combustion phase in a turbulent jet ignition process.

3. Computational setup

3.1. Model description

All numerical results presented in this paper were obtained using the CONVERGE 3.1 code, employing the Reynolds-averaged Navier-Stokes (RANS) approach, which provides an optimal trade-off between result accuracy and computational cost. The density-based PISO method was applied to solve the conservation equations for compressible flow. To reduce computational time, single-species diffusion properties were used without affecting numerical accuracy, due to the assumption of a perfectly homogeneous mixture in the combustion chamber. This section provides additional details about the sub-models used in the simulations. The renormalization group (RNG) k-ε model was used to predict the turbulent flow, which is critical in turbulent jet ignition with a passive pre-chamber [29]. The O'Rourke heat transfer model was applied to estimate wall heat losses during the cycle. This model needed to be accurate, as the experimental tests were conducted with cold engine walls due to the cool-down interval. All simulations were performed using the ECFM turbulent combustion model developed by Colin et al. [30,31], which was employed to investigate the predictive capabilities under varying hydrogen concentrations and two different equivalence ratios. The models chosen for the simulations are listed in the Table 3. Mesh generation was performed automatically at each timestep, starting from a base mesh size of 6.4 mm and refining it using

Table 2
Engine characteristics and fuel mixture properties.

Experimental conditions	
Engine Speed	900 rpm
Bore	102 mm
Stroke	105 mm
Compression ratio	13.9
Valve closing temperature	358 K
Initial pressure	0.14 MPa
Equivalence Ratio ϕ	1, 0.625
Hydrogen Ratio (percentage by volume) *HR*	0.25, 0.5, 0.75, 1

Table 3
Numerical models description.

Description	Models and mechanisms
Turbulence	RANS RNG k-ε model
Wall heat transfer	O'Rourke heat transfer model
Combustion model	ECFM
Ignition	ISSIM
Kinetic mechanisms	C3 V3.5, GRI-Mech 3.0

both available refinement systems. Adaptive Mesh Refinement (AMR) was applied locally in regions with high velocity and temperature gradients. Specifically, the flame front region, characterized by high-temperature gradients, was refined to a minimum mesh size of 0.2 mm. Additionally, local fixed embedding was implemented to improve the prediction of flame propagation, achieving a minimum cell size of 0.1 mm around the spark and within the nozzle as indicated in [32]. Table 4 provides a detailed representation of all the refinements adopted during the combustion simulations.

In Fig. 4, a slice illustrating the mesh refinements during the early stages of the combustion process provides a useful visualization of the combustion chamber geometry and the critical zones. The refinements shown in Fig. 4 were applied to each simulation and were selected based on best practices established in numerous studies in the literature that utilize the RANS approach to simulate premixed combustion in a pre-chamber engine [12–19,23,33]. To improve the rigor of the numerical analysis, a mesh sensitivity study was conducted to assess the influence of grid resolution on the combustion process. Fig. 5 compares numerical results obtained using three different base mesh sizes for the same operating condition (*HR* 0.5 with $\phi = 1$), using the same laminar flame speed and an identical calibration parameter. As described previously, all refinement strategies are directly linked to the base mesh size; therefore, when the base size is increased, the associated refinement levels scale proportionally. Specifically, the coarse mesh case employs a base mesh size of 8.0 mm, while the fine mesh case uses a base mesh size of 4.0 mm. As shown in Fig. 5, the three mesh configurations yield nearly identical main chamber pressure and apparent heat release rate (AHRR), indicating that the numerical results are not sensitive to grid resolution within the tested range. Further details are provided in the description of the numerical results, including a description of how the AHRR is computed. In particular, the turbulence induced by the flame jets and the flame propagation process are consistently captured, within the limitations of a RANS framework, as demonstrated by the close agreement between the numerical pressure traces (dashed lines) and the experimental measurements (solid lines). Specifically, the peak turbulent kinetic energy during the flame jet exit differs by approximately 7% between the fine mesh and the 6.4 mm mesh cases. This demonstrates that the combustion model is robust with respect to grid resolution within a RANS formulation. Based on this analysis, a base mesh size of 6.4 mm was selected as an optimal compromise between flame front resolution and computational cost. Finer mesh resolutions were not considered, as they are not appropriate within the adopted RANS approach.

Table 4
Local refinements and minimum mesh dimensions.

Mesh Description	Values
Base Mesh Size	6.4 mm
Main Fixed embedding	
Kernel Ref.1	0.1 mm
Kernel Ref.2	0.2 mm
Flame Cone 1	0.2 mm
Flame Cone 1	0.2 mm
Flame Cone 2	0.4 mm
Nozzle Ref.	0.1 mm
Adaptive Mesh Refinement	
Temperature	0.2 mm
Velocity	0.2 mm

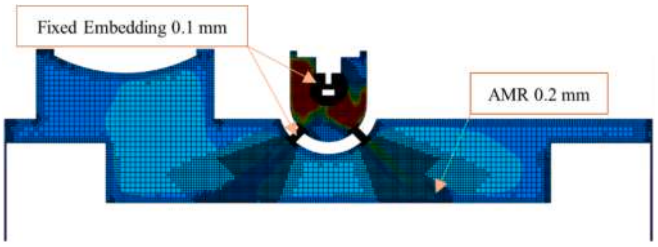

Fig. 4. Slice of the combustion simulation, illustrating the mesh structure superimposed on the temperature field.

3.2. Combustion model

In this study, a flamelet-based model was selected to describe the premixed flame combustion, aiming at reducing computational time without compromising simulation accuracy compared to experimental data. Specifically, this paper seeks to evaluate the reliability of the combustion model under varying flame conditions without the need for is an extensive calibration for each operating point. Furthermore, the study highlights potential limitations of using this flamelet model and examines the consequences of approaching these critical conditions. The ECFM for RANS relies on laminar flame speed S_l (LFS) data, which depends on the fuel properties and physical conditions inside the chamber, such as fuel concentration, pressure, temperature, and residuals. In this study, the LFS table was generated using the Chemistry tool included in CONVERGE 3.1 for all four mixtures tested in the RCEM. Additionally, two different mechanisms, GRI-Mech 3.0 from Berkeley [34] and C3 V3.5 [35], were selected to generate the LFS table through 1D simulations using the SAGE detailed kinetic chemistry model [36]. The C3 V3.5 mechanism originates from the Computational Chemistry Consortium (C3), which brings together research groups from universities, national laboratories, and industries with the shared goal of developing a unified and reliable kinetic mechanism. Furthermore, The CFD software provides the capability to extract only the species and reactions relevant to the fuels of interest. By generating the LFS table using different kinetic mechanisms, comparing numerical results with experimental data can serve a partial but necessary approach to evaluate the reliability of the kinetic models under typical engine operating conditions. Furthermore, the inclusion of optical images enhances the robustness of the model validation. Once the chemical contribution to flame propagation is defined, ECFM addresses the turbulence-chemistry interaction by incorporating a transport equation for the flame surface density. This passive is crucial for determining the reaction rate $\dot{\omega}$ by eq. (1), which in turn establishes the fuel and oxidant consumption rates.

$$\dot{\omega} = \frac{\rho_u}{\overline{\rho}} S_l \Sigma \tag{1}$$

Here, ρ_u is density of unburnt gas.

The flame surface density Σ equation (2) is defined locally and is responsible of capturing the wrinkling effect of turbulence on the flame front.

$$\frac{\partial \Sigma}{\partial t} + \frac{\partial u_i \Sigma}{\partial x_i} = \frac{\partial}{\partial x_i}\left(\frac{\mu}{Sc}\frac{\partial(\Sigma/\overline{\rho})}{\partial x_i}\right) + \left(At_{sgs} + At_{res} + Curv_{sgs}\right)\Sigma - \mathrm{D} + P_k \tag{2}$$

Omitting the classical terms that model unsteady, convection, and diffusion phenomena, we focus instead on the distinct source and sink terms, which are modelled as follows:

- $At_{sgs} = \alpha K_t$ represents the flame surface production by turbulent stretch;

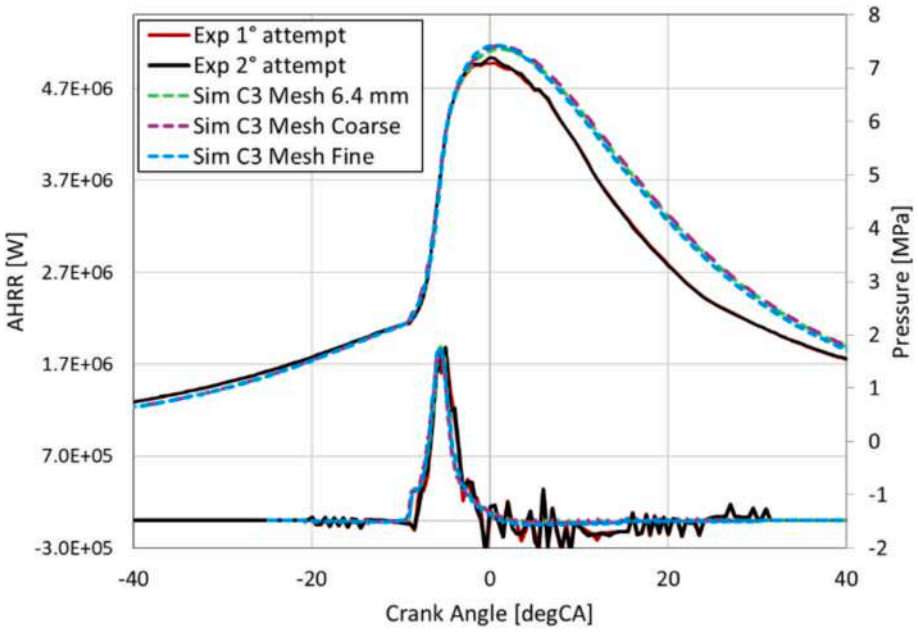

Fig. 5. Main chamber pressure and AHRR for mash sensitivity analysis.

- $At_{res} = \frac{2}{3}\frac{\widetilde{\partial u_i}}{\partial x_i}$ is the flame surface production by the mean flow dilatation;
- $Curv_{sgs} = \frac{2}{3}\frac{\rho_u}{\rho_b}S_l\frac{1-\widetilde{c_\Sigma}}{\widetilde{c_\Sigma}}\Sigma$ models the effects of the flame thermal expansion and curvature;
- $D = \beta S_l\frac{\Sigma^2}{1-\widetilde{c}}$ is the destruction term due to the fresh gas consumption;
- P_k is a source term that include the contribution of the ignition by the spark plug.

As indicated by the reaction rate expression (1), the turbulence-chemistry interaction depends, on one hand, on the laminar flame speed S_l, which is a fuel-related property. On the other hand, the flame surface density determines the turbulence contribution to flame propagation and is indirectly influenced by the fuel's characteristics. Specifically, the first source term At_{sgs} is associated with the laminar flame thickness, which varies based on the fuel properties. The term At_{sgs} consists of the adjustable parameter α and the turbulent stretch K_t, which is defined by the Intermittent Turbulent Net Flame Stretch (ITNFS) model (3).

$$\frac{K_t}{\varepsilon/k} = ITNFS_{factor}\cdot\Gamma_k\left(\frac{u'}{S_l},\frac{L}{\delta_l}\right) \tag{3}$$

$$\Gamma_k = \frac{c_{ms}}{\ln 2}\int_{scales} C_{MP}\left(\frac{r}{\delta_l}\right)\bullet\left(\frac{L}{r}\right)^{\left(\frac{2}{3}-\frac{\mu}{9}\right)} d\left[\ln\left(\frac{L}{r}\right)\right] \tag{4}$$

$$C_{MP}\left(\frac{r}{\delta_l}\right) = 10^{-c(s)} \tag{5}$$

where

$$c(s) = \frac{0.545}{s+0.364} \tag{6}$$

and

$$s = log_{10}\left(\frac{r}{\delta_l}\right) \tag{7}$$

The ITNFS model aims to characterize the stretching effect of the flame by accounting for the effective ability of different turbulence scales to perturb the flame front through strain. Eqs. (4)–(7) represents the net stretch ratio function Γ_k which correlates the turbulence scale, relative to the laminar flame thickness, with an efficiency function, C, which can be defined in various ways. The efficiency function C defines the effective deformation and wrinkling of the flame front caused by a vortex with a specific turbulent length scale. Different fuels and mixtures interact with turbulence in distinct ways, leading to flame stretching driven by different physical mechanisms. Therefore, the formulation must be adaptable to various combustion regimes, since the dominant contributions to flame stretch, such as strain and curvature, vary depending on the operating conditions. Several new formulations and modelling approaches for C have been developed to account for variations in mixture properties, with the aim of extending the validity range of the ECFM model; however, a detailed description of these methods is beyond the scope of this study. The mathematical description of C chosen for our simulations was developed by Meneveau and Poinsot [37] and is among the simplest available, though not specifically optimized for hydrogen combustion. Alternative formulations, such as the algebraic expressions proposed by Charlette et al. [38] and Bougrine et al. [39], are available in literature. These models are based on best-fit correlations from their flame/vortex DNS studies and attempt to incorporate thermo-diffusion effects through the Lewis number. Another option could be to use the latest efficiency function expression (LPF model) developed by Suillaud et al. [40], which considers the flame as a low-pass filter, cutting off turbulence scales smaller than the flame thickness. The LPF was tested and validated using the same experimental data, providing relatively good results, although the alpha stretch parameter exhibited a linear variation with changes in mixture composition [41]. All these expressions attempt to mathematically resolve the turbulence-flame interaction, extending the model's validity to other combustion regimes where turbulence penetrates the flame thickness or flame instabilities become significant. During the calibration of the combustion model, the α parameter was adjusted between different cases, serving as the tuning parameter for the combustion model. Coupled with the ECFM, the ISSIM ignition model was used to simulate the early stages of the combustion process [42].

4. Simulation procedure

Before analysing the combustion process, several cycles were

simulated with the valve open and a perfectly premixed mixture. These cycles aimed at initializing the turbulence patterns inside the combustion chamber, generated by the expansion and compression processes, as well as the tumble motion resulting from fluid-valve interaction. These initial cycles were conducted using a full geometry version to account for the inflow and outflow flux. More in detail, two different CAD models were created: the first model, which included the entire intake port and mixing tank, was used to simulate the motored cycle up to the valve closure. The second model, simplified by removing the valve and port and retaining only the combustion volume, was used to simulate the remaining part of the cycle, focusing on the combustion event.

Fig. 6 illustrates the full geometry with a slice showing the velocity magnitude during the intake process. To reduce computational time, the turbulence initialization was performed only once, using a single hydrogen ratio (*HR* 0.5 with $\phi = 1$), as varying the hydrogen concentration in the mixture would not significantly affect the motion characteristics inside the combustion chamber. After completing the motored cycles to establish a consistent flow motion for all simulations, the second phase began using a map saved just before the valve closure, at the start of the compression stroke. The primary goal of this second phase was to fit the pressure curve, particularly just before ignition. Experimental data indicated that the pressure curve during the compression stroke varied slightly between different cases. The setup changes between cases were minimal, but by using the pressure as a target value, we ensured that combustion started under the correct conditions. It is important to note that the focus of this paper was entirely centred on analysing the combustion phase in detail to evaluate the reliability of the combustion model applied to different hydrogen concentrations. The primary aim is to accurately match the chamber conditions just before the spark for all cases. After completing the second phase, the final phase involves simulating the combustion process while varying the hydrogen ratio and equivalence ratio, maintaining the same setup and adjusting the constants for turbulent stretch α that governs the turbulence-flame interaction.

5. Simulation results

5.1. Results presentation

As mentioned earlier, the primary objective of this paper is twofold. On one hand, it aims to demonstrate the potential of using the ECFM model in RANS simulations of a spark-ignition internal combustion engine equipped with a passive pre-chamber, while varying the hydrogen concentration in methane. On the other hand, relevant experimental data are utilized to validate the simulation results and highlight the effects of higher hydrogen concentrations in a methane engine, even with a lean mixture. Beyond the primary objective, this study provides an opportunity to explore how different combustion regimes, associated with different hydrogen concentrations and equivalence ratios in the mixture, interact with the phenomenology of the flame propagation both in experiment and numerical. Additionally, it is worthwhile to assess the performance of a flamelet model across a range of flame characteristics resulting from the diverse mixture compositions. Moreover, the pre-chamber system allows the investigation of two different combustion processes during the same combustion event. All the parameters used to analyse the combustion process were derived from these obtained values, applying the same methodology to both numerical and experimental data to ensure consistency throughout the analysis.

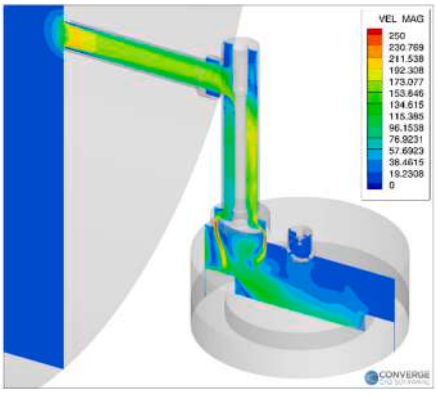

Fig. 6. Initial cycles simulation establishing the turbulence field through the exchange of the mixture between the mixing tank and the combustion chamber.

Using the pressure and volume data relative to the crank angle, the Apparent Heat Release Rate (AHRR) can be computed consistently for both numerical and experimental data through the application of the first law of thermodynamics (5).

$$AHRR = \frac{\partial Q_a}{\partial \theta} = \frac{k}{k-1} p \frac{dV}{d\theta} + \frac{1}{k-1} V \frac{dp}{d\theta} \tag{8}$$

The crank angle interval for calculating the Apparent Heat Release Rate is restricted to a short time period to minimize disturbances caused by the pressure drop described below. Integrating the AHRR values provides the cumulative heat release (CHR) (6), which can further be used to compute the mass fraction burnt (MFB) (7).

$$CHR = \int_{\theta in}^{\theta fin} AHRR d\theta \tag{9}$$

$$MFB(\theta) = \frac{CHR_\theta}{CHR_{MAX}} \tag{10}$$

Furthermore, the derivative of the pressure in the main chamber was calculated to determine the maximum derivative values and facilitate a comparison between the experimental and numerical results. In the final phase, the Damköhler number (8) and Karlovitz number (9) were computed to construct the Borghi-Peters diagram, enabling correlation of the numerical and experimental results with the respective combustion regimes.

$$Da = \frac{s_l}{u'} \frac{L_t}{\delta_l} \tag{11}$$

$$Ka = \frac{\sqrt{Re_t}}{Da} \tag{12}$$

where L_t is the turbulent length scale, δ_l is the laminar flame thickness, and Re_t is the turbulent Reynolds number. Additional secondary parameters are included in the supplementary material to further evaluate the agreement between experimental and numerical results, highlighting the differences between the two mechanisms. As pointed out previously, ECFM model required a laminar flame speed (LFS) table to correctly compute the burning rate and the flame propagation. Fig. 7 presents the laminar flame speed results, comparing the two mechanisms across both equivalence ratios examined in the combustion process.

The solid line represents the values obtained from C3 V3.5, while the dashed line corresponds to those from GRI-Mech 3.0. Chart **a** illustrates a stoichiometric mixture at 4 MPa pressure, whereas chart **b** represents a lean mixture ($\phi = 0.6$) at the same pressure. The α stretch parameter was calibrated based on the LFS table generated from the C3 V3.5 mechanism, and the same parameter was applied to simulations using the GRI-Mech LFS table. This approach ensures a consistent comparison to evaluate which LFS table aligns more closely with the experimental combustion rate varying the mixture characteristics.

5.2. Calibration process

The same procedure was applied across all cases to ensure consistent and reliable results. Since the flame stretch model struggles to correctly

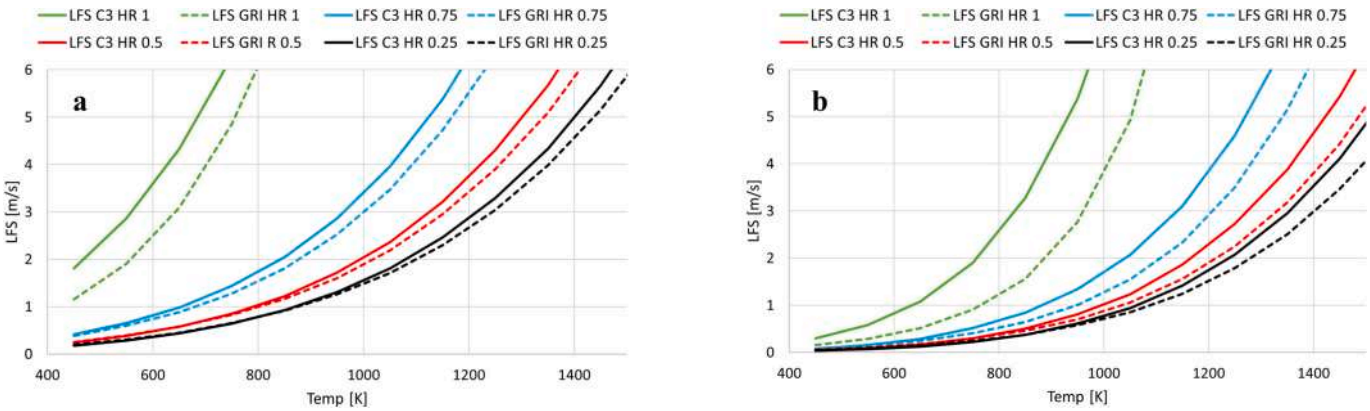

Fig. 7. Laminar flame speed values generated from the C3 V3.5 and GRI-Mech 3.0.

compute the flame stretch across different combustion regimes due to variations in mixture composition, the alpha stretch calibration compensates for these errors and enables the assessment of the model's predictive capability.

In Fig. 8, the chart illustrates the variation in alpha stretch values with changing hydrogen concentrations for the two equivalence ratios. As shown in the chart, lower hydrogen concentrations generally require higher alpha stretch values to align with experimental data. Stoichiometric cases exhibit relatively stable alpha stretch values across varying hydrogen ratios, with values ranging between 1.4 and 2.0. In contrast, lean cases display greater variability, with alpha stretch values increasing significantly as hydrogen concentration decreases, ranging from 1.5 to 3.2. The alpha stretch variation can be directly correlated with the combustion properties described by the Borghi-Peters diagram. The alpha stretch calibration, unfortunately, is insufficient to achieve perfect results in flame propagation prediction, This is likely due to the limited accuracy of the reaction mechanisms in predicting the laminar flame speed in such a wide range of hydrogen concentration and equivalence, or to the stretch model's lack of adaptability when the combustion regime changes. Another effective approach to evaluate the error in predicting laminar flame speed behaviour is by comparing the numerical results of pre-chamber pressure with the pressure data acquired from the sensor located inside the pre-chamber. The pressure spikes in the pre-chamber data serve as a valuable reference for verifying the spark timing accuracy of the simulations against experimental results and assessing the combustion model's performance in predicting flame propagation within the pre-chamber, as shown in Fig. 9. The black and red curves represent two separate repetitions of the same experiment conducted under identical mixture conditions, following a cool-down phase between them. All the figures presented in this paper will maintain a consistent structure to ensure better representation and

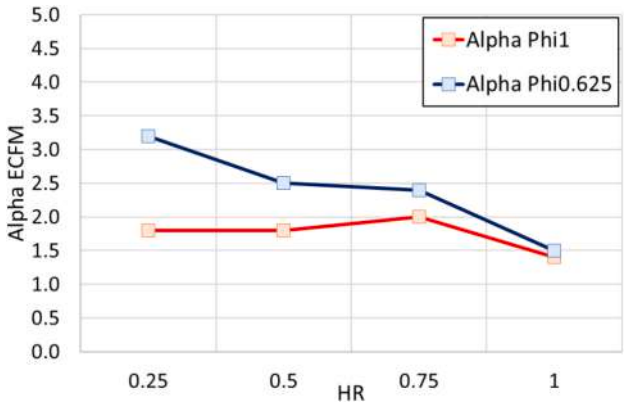

Fig. 8. Alpha stretch values used in the calibration process of the ECFM model.

improved clarity. Varying the hydrogen concentration reveals a trend where cases with lower hydrogen ratios exhibit an anticipated behaviour forced by the extreme calibration of alpha stretch value. This may occurs because the lack of accuracy in laminar flame speed prediction necessitates a calibration process that artificially advances the combustion process to align with the main chamber pressure curve. However, varying the chemical properties of the mixture could impact the effectiveness of the flame stretch model in capturing turbulence-chemistry interactions, potentially reducing its accuracy in predicting the effects of different hydrogen concentrations. If the goal were to fit the initial spike in pre-chamber pressure, it would lead to an underestimation of the pressure rise in the main chamber, resulting in an entirely inaccurate combustion prediction. This trend is particularly pronounced in lean cases, where significant discrepancies in pressure peak timing are observed. The cases with the lower hydrogen concentrations experienced slower combustion propagation within the pre-chamber in non-calibrated case, which affected both the timing of the flame jet and the pressure increase. The pre-chamber results emphasize the importance of accurately simulating flame evolution in the pre-chamber to ensure correct prediction of the main-chamber combustion event. This will become evident when analysing the optical images, which visually compare the flame propagation and jet exit through the nozzles between the numerical results and the experimental data. For each case, four distinct crank angles are shown, comparing the experimental images with corresponding visualizations of the 3D outputs obtained from CFD simulations. These simulation images provide valuable insights into flame evolution, allowing a direct comparison of the two different LFS tables. The images are included as supplementary material due to the extensive number of experimental and numerical images obtained for each case. They allow for a detailed evaluation of the initial phase of the combustion process, which is visible through the RCEM's glass window. The optical images were captured through the central section of the piston, focusing solely on the initial phase of combustion in the main chamber. This sequence captures the moment the flame jets emerge from the nozzles until the flame fully extends and attaches to the glass insertion. By correlating the crank angles visible in the optical images with the MFB charts, it is evident that these images represent only the early stages of the combustion process, when the flame begins to propagate. More specifically, qualitative observations can be made by comparing the optical images of the numerical results with the experimental data.

Examining systematically, the *HR* 1 cases (both stoichiometric and lean) demonstrate excellent alignment in the timing of the flame jet exiting from the nozzles. This alignment corresponds well with the numerical start timing and the experimental ignition confirmation, demonstrating the model's effective adaptation to low- and high-turbulence pure hydrogen combustion across varying equivalence ratios. Notably, in the lean cases ($\phi = 0.625$), the GRI-Mech 3.0 results

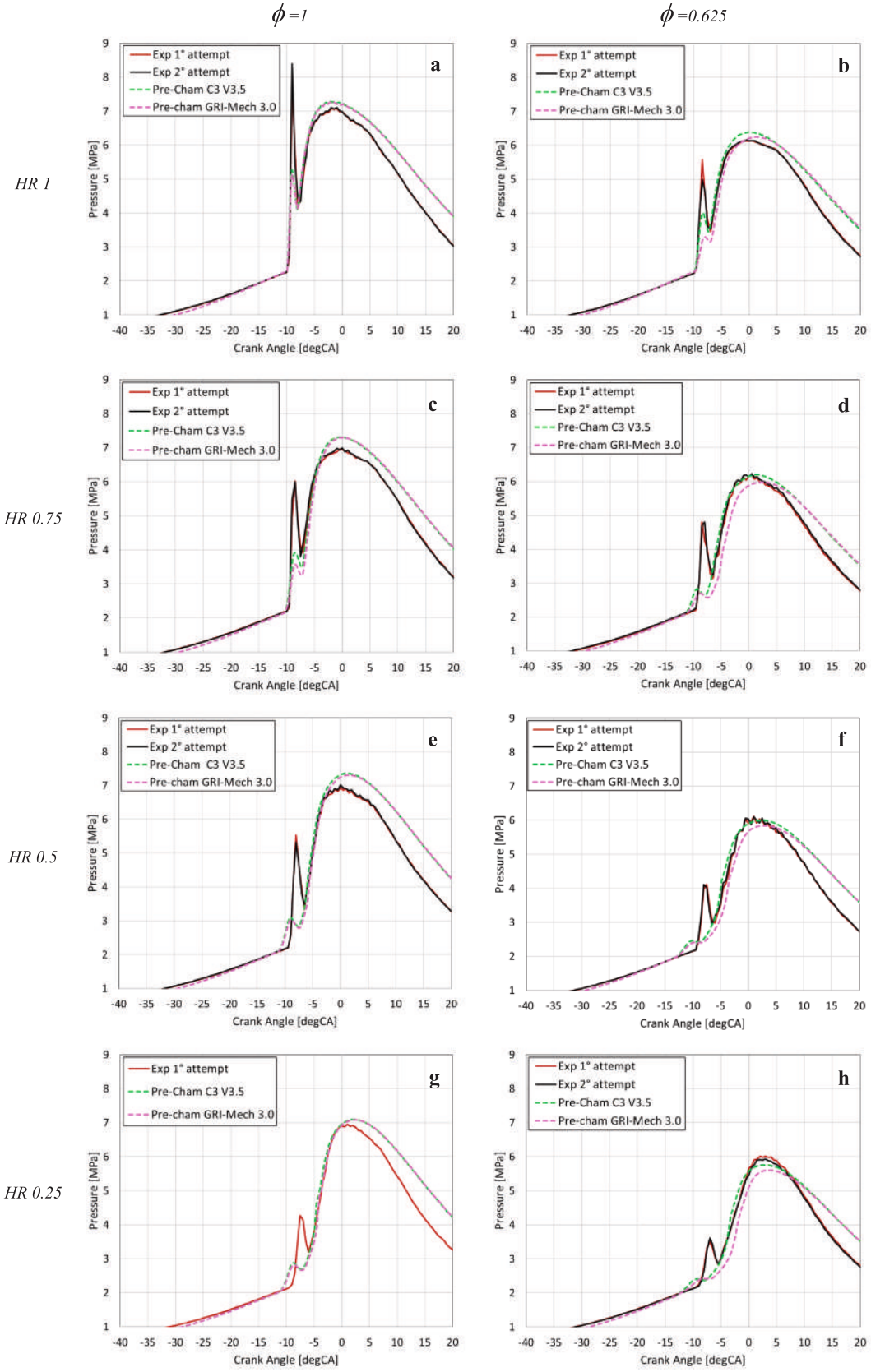

Fig. 9. Pre-chamber pressure comparison between experimental data and numerical results for both mechanisms adopted.

deviate significantly from both the C3 V3.5 results and the experimental data, showing even worse adaptation to alpha stretch increase. This discrepancy highlights that the GRI-Mech mechanism may not be optimized for lean combustion as its laminar flame speed values are significant slower compared to the values from C3 V3.5, which align more closely with the experimental observations in general. In parallel, in particular for pure hydrogen cases, the strong agreement between numerical and experimental data is further evidenced by the minimal increase in the alpha stretch of the ECFM model when transitioning from stoichiometric to lean conditions (from 1.4 to 1.5). Moving forward, the *HR* 0.75 case demonstrates good overall alignment with the experimental data. In the stoichiometric cases, both GRI-Mech 3.0 and C3 V3.5 exhibit nearly similar behaviour when compared to optical images, although GRI-Mech 3.0 shows a slightly slower flame propagation. The flame ejection timing aligns well with experimental observations as also will be shown in the pressure curve and MFB charts. In contrast, the lean cases reveal notable differences, with the numerical flame exiting occurring approximately 1° CA earlier to compensate for the slower burn rate in the main chamber. The lean cases highlight disparities between GRI-Mech 3.0 and C3 V3.5, particularly in the initial stages of combustion and lower hydrogen content. The combustion model generally underestimates the burn rate, resulting in slower flame propagation. Similarly, the *HR* 0.5 case yields results comparable to the *HR* 0.75 case, further exaggerating the discrepancies in flame jet delay and the underestimation of the burning rate during flame propagation within the main chamber. In contrast to the lean cases, the stoichiometric cases exhibit less pronounced differences between the two mechanisms applied to the combustion model. Two cases are reported explicitly in this paper in Fig. 10 to visualize the correspondent observation, the first with *HR* 1 and the second having *HR* 0.25 that represent the opposite cases concerning the hydrogen concentration. For each case, three columns are available as in supplementary material, corresponding to three different results for the same condition. The central column displays the experimental optical images, while the left and right columns show the numerical results. Specifically, the right column corresponds to results obtained using the GRI-Mech 3.0 mechanism, and the left column represents results generated by the C3 V3.5 mechanism, calibrated in the same way. All images were selected to correspond to the same crank angle degree across the different cases, except for the first row. In that row, the numerical images were chosen to capture the moment of the flame jet exit in each case, in order to clearly highlight the timing discrepancies between the cases. In more detail, the camera acquisition relies on the shadowgraph technique to trace the flame front inside the main chamber. This method visualizes density gradients in transparent media, and variations in the refractive index allow the identification of different temperature regions, making the flame front distinguishable. The white line highlights the discontinuity in gas temperature, clearly marking the evolution of the flame front within the visualized plane of the main chamber, enabling an easier comparison with the numerical images.

These two cases were selected to better visualize the key observations derived from the pressure curve analysis and the other figures presented earlier. The optical image comparisons reveal two distinct characteristics. Notably, differences in flame propagation speed are evident between the two mechanisms, with GRI-Mech 3.0 exhibiting a repeated lower laminar flame speed compared to C3 V3.5 as shown in Fig. 7 in lean mixture. Additionally, while the pure hydrogen mixture (group **a**) demonstrates excellent alignment between experimental and numerical timing, discrepancies in flame jet exiting are observed in the *HR* 0.25 case, reflecting challenges in matching experimental results in mixtures with low hydrogen concentrations. It is also evident in group **b** that there is a significant underestimation of the flame propagation speed within the main chamber when comparing the C3 V3.5 results to the experimental images, which display a faster evolution and propagation of the flame. These differences may arise from variations in laminar flame speed caused by differing hydrogen concentrations and the lower optimization of both mechanisms in lean methane mixtures. More specifically, the underestimation of the laminar flame speed may leads to slower flame jets exiting the orifices, which also results in an underestimation of the turbulence induced by the jets. Consequently, this predicts a slower burn rate in the main chamber. The optical images offer valuable insight into the combustion analysis, providing a more detailed understanding of the combustion process, capturing the multiple-point ignition inside the main chamber. While there is room for improvement in accurately capturing the initial phase of combustion, the current level of accuracy was deemed sufficient for this initial study.

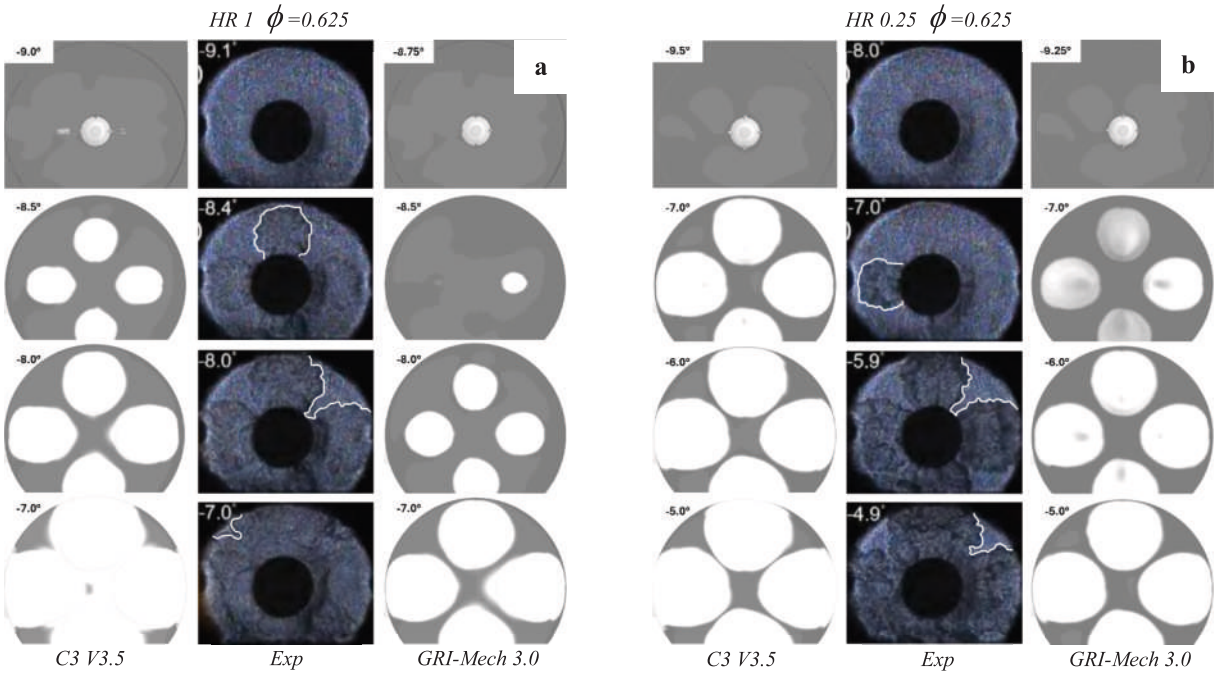

Fig. 10. Optical images for two different cases representing the evolution during the combustion cycle in crank angle degree. The left group (a) represents the case with $HR = 1$ and $\phi = 0.625$, while the right group (b) shows the case with $HR = 0.25$ and $\phi = 0.625$.

In the stoichiometric case, both mechanisms perform similarly, as evidenced by the alignment in flame propagation images. However, the lean case highlights limitations evident when comparing the laminar flame speed tables at lean equivalence ratios, revealing the challenges in accurately predicting lean methane/hydrogen combustion, particularly at low hydrogen ratios, due to the low fidelity of the mechanisms couple with a lack in turbulence-flame interaction prediction modelled by the flame stretch model. More in detail, as presented in the combustion characterization chapter, the main source of modelling error arises from variations in the Karlovitz number, which lead to changes in the combustion regime. As the regime shifts, the mechanisms governing turbulence-chemistry interaction alter their influence on flame propagation, modifying the role of turbulence on the flame. Since the combustion model is based on the flamelet concept, it is not designed to accurately capture such phenomena, and modelling errors are therefore expected.

5.3. Model validation

Fig. 11 presents the numerical and experimental comparisons of pressure in the main chamber and the apparent heat release rate (AHRR) across all eight simulated cases. For each case, the two laminar flame speed (LFS) tables, derived from the different kinetic mechanisms already introduced, were tested using the same setup. The left column will always display the stoichiometric cases, starting from *HR* 1 at the top to *HR* 0.25 as the last chart at the bottom. In the right column, the lean cases are presented, with each row corresponding to the respective hydrogen ratio shown in the left column. The charts clearly demonstrate the significant impact of higher hydrogen concentrations on both pressure and heat release. Specifically, higher hydrogen concentrations provides a faster combustion, an higher pressure peak, and a steeper pressure gradient, as evidenced by the AHRR curves for both stoichiometric and lean mixtures. This is evident when comparing chart **a** to chart **g** in the left column, as the mixture transitions from pure hydrogen to 25% hydrogen by volume relative to methane. A similar observation can be made by evaluating the right column, from chart **b** to chart **h**. Generally, the experimental trend is captured well by the numerical results varying both the hydrogen content and equivalence ratio. The numerical results demonstrate better agreement in stoichiometric mixtures, while lean mixtures exhibit greater variability between simulated and experimental outcomes. This discrepancy is particularly pronounced in cases with lower hydrogen concentrations, where the mixture is almost entirely dependent on methane flame propagation.

Before delving into the results in detail, it is helpful to explain the discrepancies observed during the expansion stroke, as seen in the comparison of the pressure curves between numerical and experimental data. The pressure drop during the expansion stroke is primarily attributed to blow-by, which significantly affects the experimental pressure measurements. This phenomenon arises due to the numerous sensors and accessories installed on the RCEM, as well as the unique piston ring design, which cannot ensure optimal sealing of the combustion chamber. Despite efforts to isolate all sensors and inserts to mitigate this issue, a non-negligible blow-by was still observed during operation, both in compression and expansion stroke. The analysis presented in this paper is not influenced by these losses, as the evaluation of the combustion process is confined to a short crank angle range defined by the AHRR crank angle range. Therefore, the analysis, supplemented by optical access images, remains consistent and reliable. From Fig. 11, it can be observed that simulations using the C3 V3.5 mechanism generally produce better results compared to those using GRI-Mech adopting the already mentioned flame stretch model, particularly under lean conditions. In stoichiometric conditions, however, the results are quite comparable between the two mechanisms. Specifically, for lean mixtures with higher hydrogen concentrations, the C3 V3.5 mechanism performs notably well, likely due to its greater optimization for hydrogen combustion. The flame speed propagation is slightly faster in the C3 V3.5 cases compared to the GRI-Mech cases. This observation aligns with the laminar flame speed table charts displayed in the Fig. 7, which consistently show higher flame speed values for the C3 V3.5 mechanism than for GRI-Mech, especially in the lean mixture. These differences in laminar flame speed values result in varying flame propagation dynamics within the pre-chamber, with higher hydrogen concentrations leading to increased flame speeds. The flame propagation inside the pre-chamber influences the flame jets exiting through the nozzles, generating high turbulent kinetic energy based on the jet propagation characteristics. Faster jet ejections result in higher turbulence intensity, which subsequently accelerates the combustion process in the main chamber due to the combined effects of elevated laminar flame speed, driven by hydrogen content, and increased turbulence intensity [4,7,25,26]. This observation holds because, prior to spark ignition, the turbulence levels are approximately the same across all simulated cases. The tables included in the supplementary material show the differences in engine parameters between the two mechanisms for each case. To gain a deeper insight into the flame propagation characteristics and assess the model's performance in predicting flame speed and burn rate, Fig. 12 proves helpful by visualizing the mass fraction burnt (MFB) for each case. This comparison provides a clearer representation of the combustion progression and highlights the differences between the mechanisms and mixture conditions. As anticipated in the AHRR charts, the MFB plots reveal an almost perfect agreement in the combustion rate for stoichiometric cases. However, lean mixtures present more challenges in achieving accurate predictions, particularly at lower hydrogen concentrations. These discrepancies will be further analysed through a combustion regime evaluation, assessing whether the cases remain within the flamelet regime or transition into more critical conditions.

In more detail, for the lean cases, C3 V3.5 exhibits an earlier combustion phase, as indicated in the MFB charts, despite both mechanisms sharing the same spark timing and alpha stretch value. This aligns with the previously discussed analysis of the optical images, which capture the initial phase of the combustion process in the main chamber. Again, this behaviour could be attributed to a faster combustion process occurring within the pre-chamber, potentially caused by discrepancies in laminar flame speed values or differences in turbulence interaction due to variations in the alpha stretch values. Furthermore, Fig. 12 clearly demonstrates the increase in the combustion rate with higher hydrogen concentrations, as evident from the steeper slopes of the MFB curves. Notably, even a small amount of hydrogen (case *HR* 0.25) is sufficient to sustain a favourable combustion rate in a lean methane mixture, highlighting hydrogen's significant impact on enhancing flame propagation in such conditions. This observation clearly demonstrates the beneficial role of TJI combustion in lean and ultra-lean conditions, effectively enhancing combustion efficiency while promoting cleaner combustion. To summarize the results, it is useful to introduce a numerical and experimental correlation analysis that highlights the shared trends. Specifically, the experimental data from one of the two repetitions can be compared with the simulated data, focusing on the results obtained using the C3 V3.5 mechanism, which was chosen for its better alignment with lean mixture conditions.

In Fig. 13, the simulation results demonstrate a consistent trend with the experimental data when varying the equivalence ratio and hydrogen concentration, showing no significant errors. Once more, the warm colours correspond to the stoichiometric cases, while the cold colours represent the lean mixtures, also highlighting the experimental uncertainties arising from the pressure acquisition resolution. Notably, the chart **b**, which displays the crank angle corresponding to the maximum pressure derivative highlights the influence of flame speed on combustion flame propagation due to the hydrogen concentration in the mixture due to the experimental trend followed by the numerical results. In other words, while maintaining nearly the same maximum pressure and spark timing across all cases, a delay in the crank angle of maximum pressure derivative becomes evident as the hydrogen ratio decreases. This delay

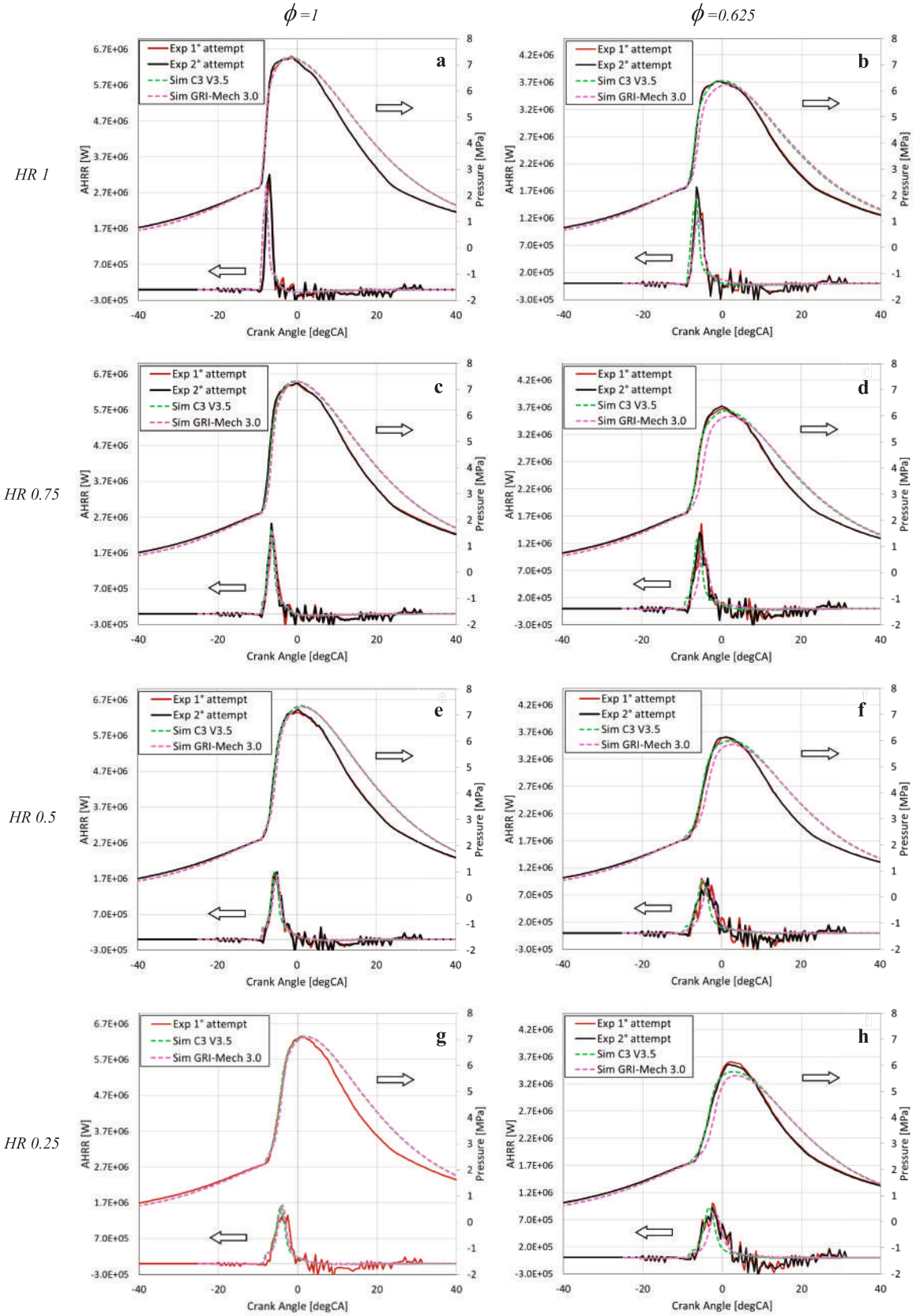

Fig. 11. The main chamber pressure curve and AHRR are represented in green for C3 V3.5 and pink for GRI-Mech 3.0. Charts (a-c-e-g) correspond to the stoichiometric cases, while charts (b-d-f-h) represent the lean cases. (For interpretation of the references to colour in this figure legend, the reader is referred to the web version of this article.)

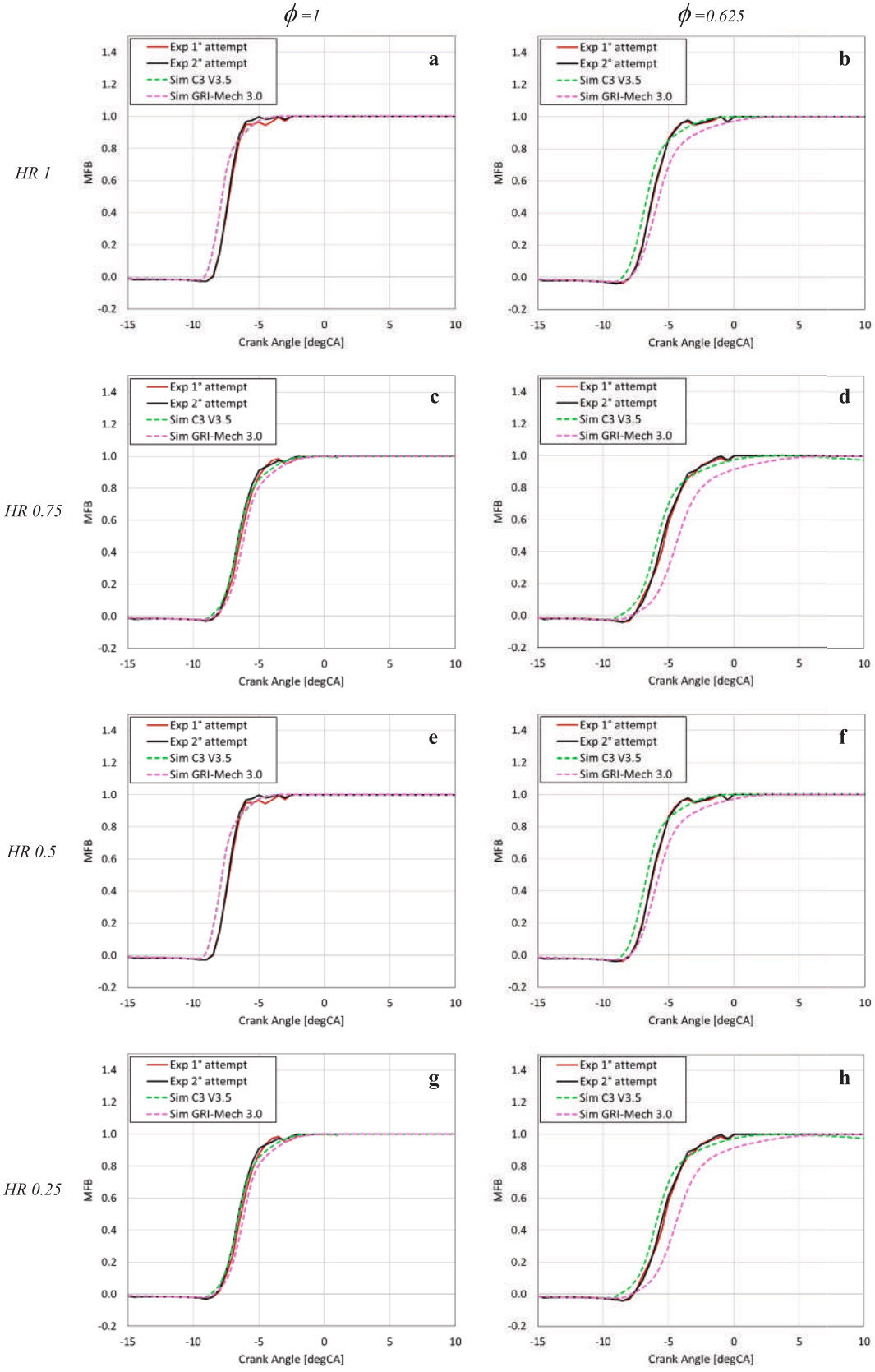

Fig. 12. Mass fraction burnt, comparing the simulation results (dashed line) with the experimental results (solid line).

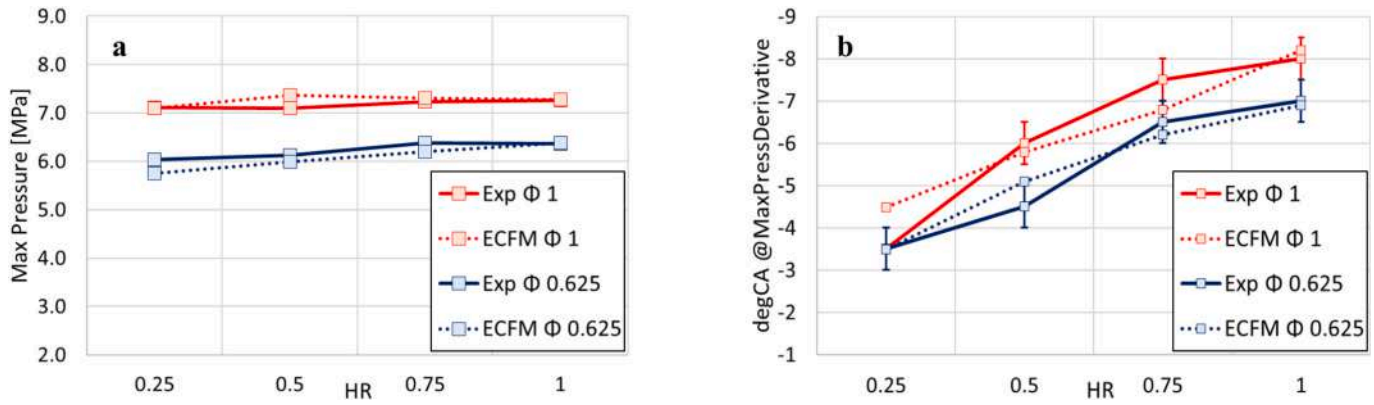

Fig. 13. The chart **a** displays the maximum pressure values. The chart **b** shows the crank angle values corresponding to the maximum pressure derivative during the combustion cycle.

is attributed to reduced mixture reactivity that leads to a slower turbulence induced by the flame jet as a result of the lower hydrogen concentration. Specifically, the chart **a** of Fig. 13 illustrates strong alignment between the simulation results and experimental data, further validating the accuracy of the combustion model. The increase in hydrogen concentration enhances the laminar flame speed and the fuel's reactivity, resulting in faster combustion and a more rapid pressure rise but the maximum values remain almost constant. Instead, notable differences emerge between stoichiometric and lean cases, highlighting how the combustion dynamic is influenced by the equivalence ratio. The chart **b** in Fig. 13, as previously described, serves as an indicator of how quickly the combustion occurs and highlights the steepest point of the pressure curve during the combustion process. The numerical results align with the experimental trends, showing a decline in combustion rapidity as the hydrogen content in the mixture decreases, although discrepancies become evident in cases with low hydrogen content. This is evident from the intersection of the numerical curves (dashed lines) with the experimental curves (solid lines). These intersections indicate a lack of perfect alignment due to an underestimation of the laminar flame speed, which is partially compensated for by the calibration process. It is important to clarify that all the indicators presented so far refer to the main chamber parameters, as the influence of the pre-chamber volume is negligible compared to that of the main chamber.

Fig. 14 presents two additional indicators that characterize the simulation results (light shades) in terms of combustion duration for a specific range of mass fractions burned, validated against the experimental data (dark shades). The chart **a** illustrates the combustion duration in crank angle between the points corresponding to 10% and 90% of the mass fraction burnt. This indicator provides valuable insight into the duration of the main combustion phase, capturing the bulk of the combustion process and its progression. The main trend is effectively captured by the simulation results, though some differences arise due to the extremely rapid combustion duration. This leads to a relatively higher error between simulation and experimental data, partly due to the low experimental resolution during pressure acquisition, which is limited to 0.5 Crank Angle Degree (CAD). This further highlights the uncertainties in the numerical-experimental comparison. Despite this, the simulations accurately reflect the increase in combustion duration, aligning with the experimental trend and demonstrating the model's capability to capture the effects of varying equivalence ratios and hydrogen concentrations. Similarly, the chart **b** illustrates the combustion duration between two different mass fractions burnt (0% and 5%), providing insights into the model's predictive capability during the initial phase of the combustion process, when the flame jets begin to exit the nozzles and ignite the fresh mixture inside the main chamber. Chart **b** could be directly linked to the optical image analysis, as it precisely captures the initial moment of flame propagation. Like the chart **a**, the simulation results presented in chart **b** align well with the experimental data and accurately capture the trend induced by varying hydrogen concentrations in the fuel mixture. Given that, all combustion simulations begin with nearly identical initial conditions in terms of turbulence and mixture physical properties as previously described. Analysing the charts as a whole, it becomes evident that as the volumetric fraction decreases from *HR* 1 toward lower hydrogen content cases, the differences in hydrogen mass fraction are not of the same magnitude across all cases. The hydrogen mass fraction variations more clearly reflect the mixture's flame behaviour than the volume fraction index. Specifically, the transition from *HR* 1 to *HR* 0.75 shows a more pronounced decrease in hydrogen content compared to the shift from *HR* 0.5 to *HR* 0.25. This trend will also become evident when analysing the u'/S_L chart. This relationship highlights the influence of hydrogen concentration on the combustion characteristics, demonstrating that mixtures with lower

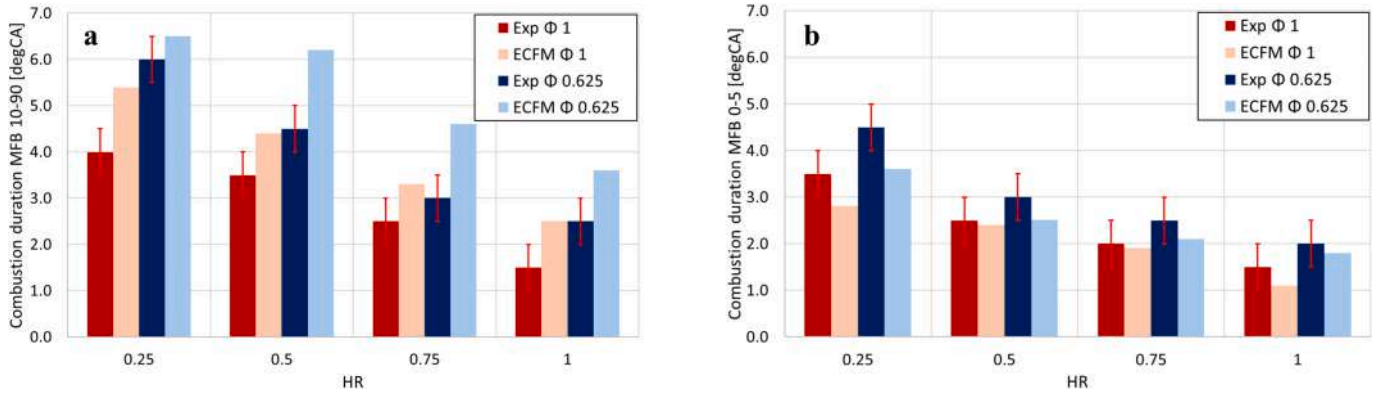

Fig. 14. Combustion duration relative to different mass fraction burnt ranges.

hydrogen content tend to exhibit comparable behaviour, particularly in terms of flame propagation and combustion dynamics, as shown in Fig. 11. The TJI system amplifies turbulence intensity due to the flame jet propagating through the pre-chamber nozzles. By comparing the laminar flame speed s_l with the root mean square (r.m.s.) of the turbulent velocity u', the chemistry-turbulence interaction in the analysed cases highlights how higher hydrogen concentrations alter combustion properties, thereby influencing the reliability of the combustion model. The Borghi-Peters diagram will be utilized to examine how variations in mixture composition and equivalence ratio influence the subsequent combustion process. This analysis aims to determine whether it is possible to correlate different combustion regimes and properties with the calibration adjustments made to align the model with experimental data.

5.4. Combustion characterization

After having clarified all the fundamental aspect of how the simulations were obtained in this study, it's time to extend the analysis further to link the calibration process and the simulation results with different combustion regimes and properties. The analysis has demonstrated that the combustion model performs differently across cases, with the calibration process emphasizing the effects of varying hydrogen and equivalence ratios. The primary challenge was observed in the lean mixtures, where the results showed greater discrepancies compared to experimental data, generally underestimating flame speed propagation. One potential explanation for these discrepancies can be clarified through the Borghi-Peters diagram (Fig. 16) and the Karlovitz number chart (Fig. 15a), which illustrate the combustion regimes and provide insight into the flame propagation characteristics.

Specifically, by plotting the Karlovitz number for each case at the point of 50% Mass Fraction Burnt (MFB 50), it becomes possible to assess whether the case adheres to flamelet combustion properties [33]. The proximity of the Karlovitz number to unity serves as a critical indicator, determining whether the combustion remains within the flamelet regime or deviates from it. It should be noted that Fig. 15 refers exclusively to the main-chamber combustion process and does not account for the combustion regime within the pre-chamber. This evaluation also provides insight into the reliability of the ECFM model under varying mixture conditions and, consequently, different combustion regimes. Values closer to unity typically indicate reduced adherence to flamelet behaviour, thereby limiting the model's applicability under those conditions. As visible in the alpha stretch chart in Fig. 8, the values align with the Karlovitz number (Ka) at MFB 50, supporting the theory that as Ka values approach unity, the flame deviates from classical flamelet properties. This deviation necessitates a more significant calibration of the alpha parameter in the model. Additionally, the chart **b** in Fig. 15 offers another perspective on turbulence-chemistry interaction. It illustrates the variations in laminar flame speed across the cases, compared with the velocity fluctuations caused by the turbulence induced by the jets exiting the orifices.

Analysing Fig. 17, which illustrates the velocity fluctuations during the combustion process in the main chamber, it becomes evident that flame propagation is influenced by the laminar flame speed, which increases turbulence intensity proportionally to the exit velocity of the flame jets through the nozzles. Specifically, Fig. 17 shows that turbulence intensity remains consistent across all cases before ignition, with differences in flame propagation arising solely from variations in the mixtures once the combustion process in the main chamber begins. The figure presents two cases with differing equivalence ratios, showcasing extreme hydrogen ratios to evaluate their impact on flame propagation and turbulence induced by the flame jets. As expected, the stoichiometric cases generate higher turbulence intensity than the corresponding lean cases due to higher laminar flame speed, which results in faster jet ejection and greater turbulence induction. Fig. 17 can be directly linked, on one hand, to the Borghi-Peters diagram, demonstrating that despite the high turbulence intensity observed in cases with high hydrogen content, this phenomenon primarily results from the extreme reactivity of the mixture, characterized by very high laminar flame speed values. As previously explained, the increased turbulence intensity is a consequence of the enhanced reactivity of the mixture, driven by the flame ejection through the orifices. On the other hand, Fig. 17, when analysed alongside Fig. 15b, further reinforces the correlation between the increase in mixture reactivity, whether due to a higher hydrogen content or a higher equivalence ratio, and the turbulence intensity in the main chamber, which is primarily induced by the combustion process occurring inside the pre-chamber. As previously noted, the initial u′ values remain consistent across the cases due to the nearly identical initial turbulence conditions. Building on these considerations, the comparison between the Karlovitz number chart in Fig. 15a and the Borghi-Peters diagram in Fig. 16 reveals that decreasing the hydrogen concentration, along with shifting from stoichiometric to leaner mixtures, results in a transition toward the thickened reaction zone TRZ. In this regime, the flamelet hypothesis seems no longer valid. More in detail, for each operating point, both the pre-chamber and main chamber combustion processes are represented within the same diagram. The colour bar beside the chart, which traces the evolution of the combustion process with respect to crank angle, allows for distinguishing the discontinuity between the initial combustion in the pre-chamber (red dots) and the subsequent combustion in the main chamber (from orange to blue dots). Focusing on the Borghi-Peters diagrams, the images illustrate that the left column, representing stoichiometric cases, falls into the corrugated flame region consistent with a flamelet regime. Conversely, the lean cases, especially those with lower hydrogen concentrations, fall into the thickened flame regime.

This leads to a more diffused flame front and turbulence interacting directly with the flame's preheat zone. By analysing the diagrams as a whole, it is possible to observe how the pre-chamber combustion regime shifts relative to the main chamber process when the mixture composition varies. This shift leads to a subsequent decline in the combustion

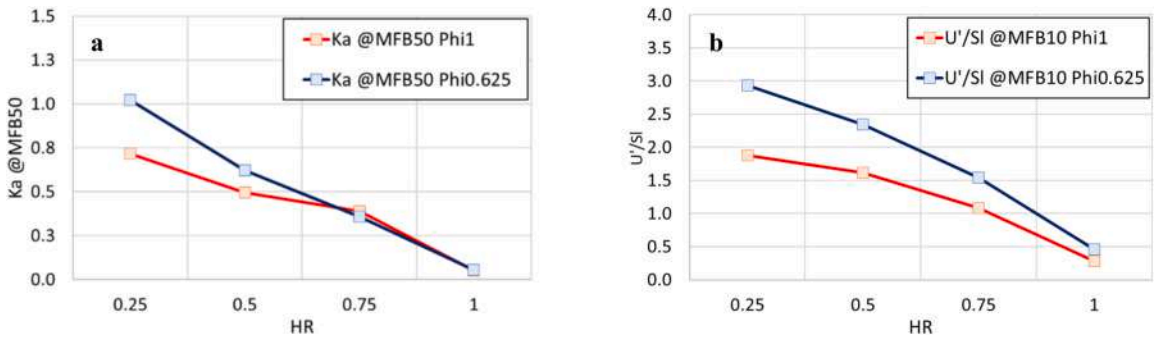

Fig. 15. The chart (a) illustrates the Karlovitz number corresponding to the crank angle at MFB 50 for the main chamber combustion process. On the right, chart (b) depicts the variation in u'/sl values as the hydrogen ratio in the fuel changes.

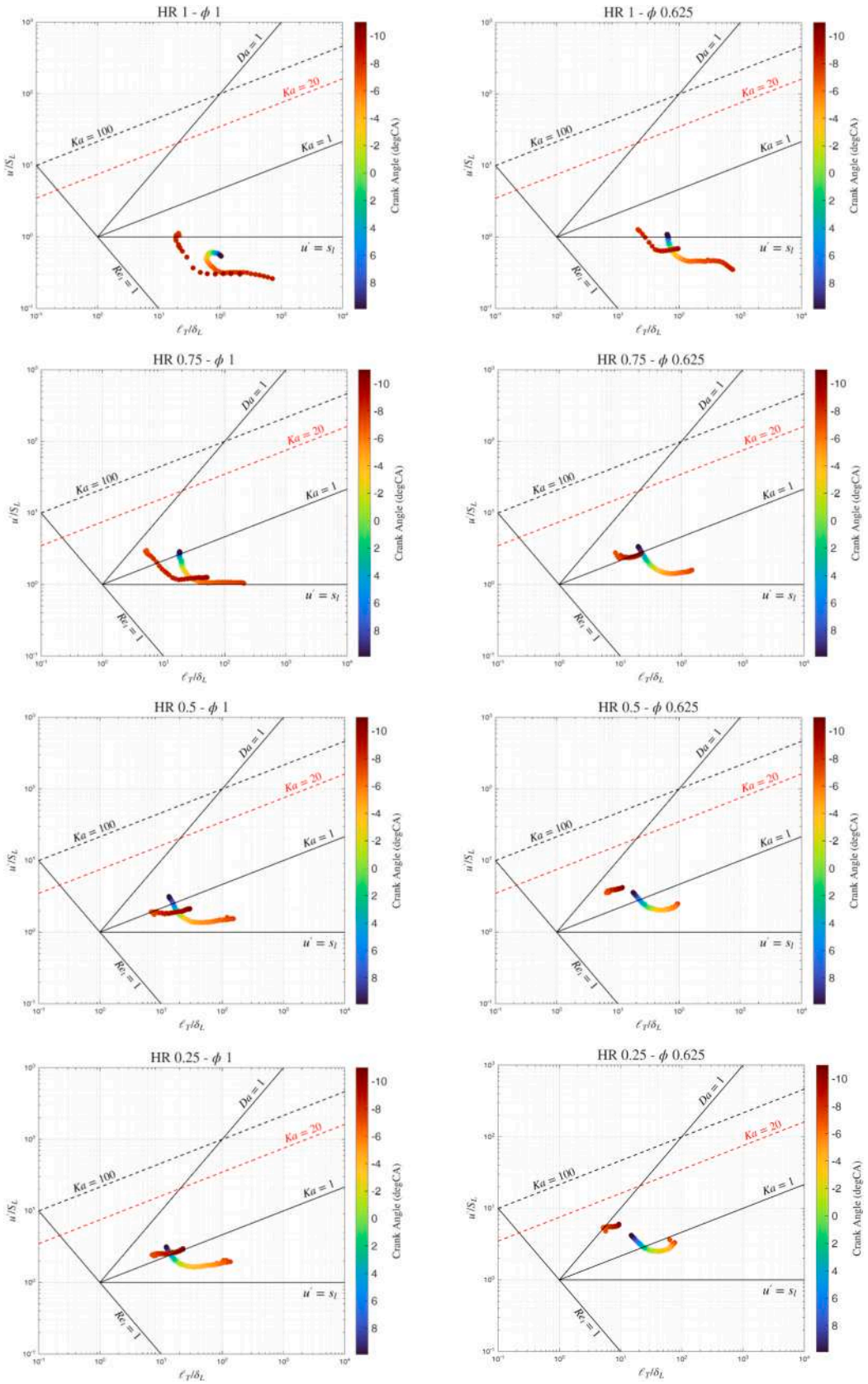

Fig. 16. Borghi-Peters diagram for each case relative to the main chamber and pre-chamber combustion process.

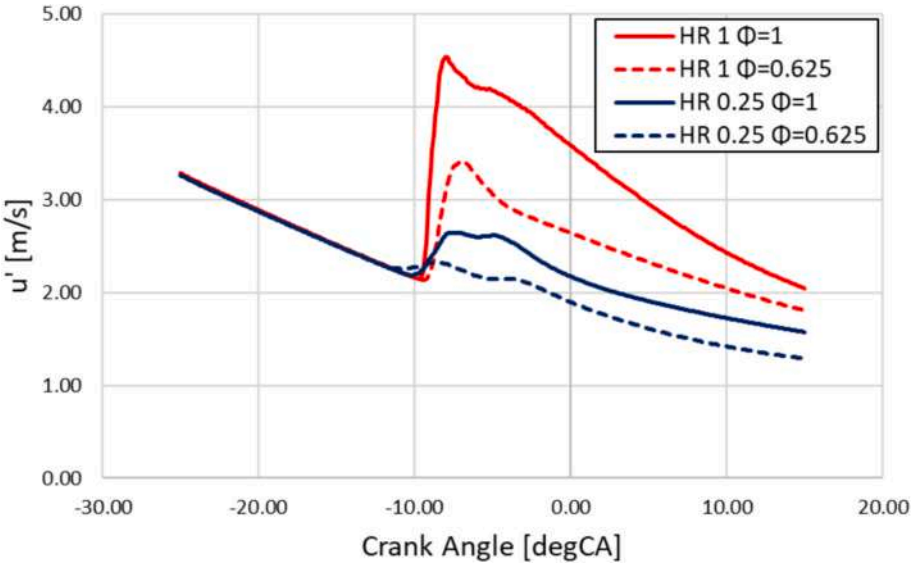

Fig. 17. Velocity fluctuations during the combustion process in the main chamber.

model's predictive capability, particularly when the pre-chamber regime enters the thickened reaction zone, corresponding to Karlovitz numbers greater than 1. These differences in combustion regimes result in distinct flame properties and behaviours in the combustion model, necessitating more complex calibration efforts of a flamelet-based model. This concept is further supported by analysing the two cases characterized by pure hydrogen mixtures, which maintain an almost constant alpha stretch value when transitioning from stoichiometric to lean conditions. This observation, along with the first row of Fig. 16, indicates that a fully wrinkled flame is well-predicted by the ECFM model without requiring extensive point-to-point calibration. In contrast, the low optimization of lean methane mixtures, combined with their departure from the flamelet combustion regime, results in poor predictive performance of the ECFM model. This is evident from the pressure analysis and the discrepancies observed in the optical images, highlighting the limitations of the model under these specific conditions, particularly in predicting flame propagation inside the pre-chamber. Some improvements were observed with the use of the C3 V3.5 mechanism compared to GRI-Mech 3.0, attributed to its better optimization for lean mixtures regardless of hydrogen concentration. However, there remains room for improvement in both the laminar flame speed values provided by the kinetic mechanisms and the representation of turbulent-flame interaction, which could be enhanced by designing an optimized flame stretch formulation that better accounts for variations in the chemical properties of the mixture, thereby enabling more accurate simulation in high Karlovitz regime. Improvements can be achieved by adopting alternative flame stretch models, such as the LPF [41], which better account for stretch effects caused by strain in high Karlovitz number regimes, leading to improved predictions of pre-chamber flame propagation. Nevertheless, despite this advancement, none of the flamelet-based models implemented in the most common commercial software are yet capable of accurately predicting flame propagation in internal combustion engines across different combustion regimes under high Karlovitz numbers.

6. Conclusion

In response to the growing interest in alternative fuels for internal combustion engines as a means of decarbonizing the transport sector, this study characterizes the performance of the ECFM combustion model under varying fuel compositions and equivalence ratios, assessing its predictive capability beyond the conventional flamelet regime. The results are directly compared with an extensive experimental campaign on a Rapid Compression Expansion Machine RCEM, which includes an optical access window in the main chamber, highlighting the influence of hydrogen enrichment in methane mixtures. The test case engine was equipped with a passive pre-chamber system that provides turbulent jet ignition to facilitate multiple-points ignition, even in lean and ultra-lean conditions. The experimental campaign provided valuable data to assess the effects of hydrogen concentration variations in a methane mixture under typical engine operating conditions, with two equivalence ratios tested for each fuel composition: a stoichiometric mixture and a leaner mixture ($\phi = 0.625$). The optical images obtained during the experimental campaign played a crucial role in validating the simulation results. They enabled a direct comparison of the flame propagation in the main chamber, highlighting the consistency between the simulated flame jets and the experimental observations captured through the glass window insertion. The variation in hydrogen ratio and equivalence ratio aimed to alter the fuel mixture's chemical characteristics, providing an opportunity to investigate turbulence-chemistry interactions while maintaining constant the initial turbulence properties. Comparing the experimental and simulation results, validated against experimental data and refined through the calibration process of the combustion model, led to the following conclusions:

- From the experimental perspective, it was observed how hydrogen addition to a methane mixture influences flame propagation, even under lean conditions, due to the turbulent jet ignition that enhances the combustion process. The pressure curves and the MFB clearly show how varying hydrogen ratios affect combustion rapidity, ensuring optimal combustion efficiency even in lean conditions for the lower hydrogen ratio case (*HR* 0.25). As expected, a higher hydrogen concentration leads to faster combustion and a steeper pressure rise, further enhanced by the turbulent jet ignition, as evidenced by the flame propagation phenomena captured through the optical access system. Furthermore, even at lower hydrogen concentrations, lean mixtures benefit from an optimized combustion process facilitated by the pre-chamber system, which enhances turbulence intensity within the combustion chamber.
- The numerical investigation aimed to assess the capability of a well-established flamelet model to predict combustion under engine-like conditions, varying the mixture composition while maintaining constant initial turbulence. Overall, the results show good model performance in stoichiometric conditions, where the flame remains

within the strict flamelet regime, specifically the corrugated flame. The model calibration exhibited a stable alpha stretch trend under these conditions. In contrast, the lean cases demonstrate that the model struggles to match experimental results even with point-by-point calibration. Furthermore, the alpha stretch parameter shows extreme variation as the hydrogen content changes. These discrepancies likely arise from shifts in the combustion regime when transitioning from pre-chamber combustion to main-chamber flame propagation. Specifically, for lean mixtures with low hydrogen content, the pre-chamber combustion enters the thickened reaction zone (TRZ), moving outside the model's validity range. For stoichiometric mixtures with high hydrogen content, both pre-chamber and main-chamber combustion remain within the corrugated flame regime, resulting in better model performance.

- For all simulations, two different kinetic mechanisms were tested to generate the laminar flame speed tables required for predicting flame propagation in the flamelet model. This approach strengthens the reliability of the numerical investigation and highlights discrepancies in laminar flame speed predictions, especially for lean mixtures. For stoichiometric cases, no significant differences were observed between the two mechanisms. In contrast, C3 V3.5 consistently outperformed GRI-Mech 3.0 in lean mixtures across all hydrogen ratios. The higher laminar flame speed predicted by C3 V3.5 helps to compensate for modelling errors and reduces the required range of alpha stretch calibration when transitioning from stoichiometric to lean conditions.
- Both observations are consistent with the validation from pressure analysis and optical access images. Comparing the numerical results with experimental flame propagation at different crank angles highlights the uncertainties in the predictive capability of the combustion model outside the strict flamelet regime, as well as the discrepancies between the two kinetic mechanisms in lean cases.

The subsequent analysis highlighted that the simulations carried out on this RCEM, validated against experimental data and optical images, demonstrate how changes in fuel properties and the fuel/air ratio impact the combustion model's ability to accurately predict the combustion process. This behaviour depends on the modelling technique used to account for variations in flame-turbulence interaction across different combustion regimes, as indicated by changes in the Karlovitz number. The sensitivity analysis using two different kinetic mechanisms demonstrates the consistency of the results across varying kinetic descriptions. This investigation provides insights into the key factors influencing flame propagation modelling and avenues for improvement. One potential enhancement involves testing alternative flame stretch models incorporating additional parameters to account for flame instability in lean and ultra-lean hydrogen mixtures. On the other hand, continuing the development of reliable chemical kinetic mechanisms validated under engine-like conditions could further enhance the accuracy and reliability of numerical analyses. New formulations are needed to extend the model's validity in high Karlovitz regimes by more accurately accounting for flame stretch effects due to strain and curvature. This would enable the study of lean and ultra-lean combustion processes while varying the mixture's chemical properties, including lower-reactivity fuels, supporting the decarbonization of next-generation internal combustion engines.

CRediT authorship contribution statement

Riccardo Sola: Writing – original draft, Validation, Software, Project administration, Investigation, Formal analysis, Data curation, Conceptualization. **Mirko Baratta:** Writing – review & editing, Validation, Supervision, Project administration, Formal analysis, Conceptualization. **Daniela Misul:** Writing – review & editing, Validation, Supervision, Project administration, Formal analysis, Conceptualization. **Fabrizio Santonocito:** Writing – review & editing, Investigation, Formal analysis, Data curation, Conceptualization. **Hiroshi Kawanabe:** Writing – review & editing, Supervision, Investigation, Formal analysis, Data curation.

Declaration of competing interest

The authors declare that they have no known competing financial interests or personal relationships that could have appeared to influence the work reported in this paper.

Acknowledgements

We acknowledge the CINECA award under the ISCRA initiative, for the availability of high-performance computing resources and support.

Computational resources provided by hpc@polito, which is a project of Academic Computing within the Department of Control and Computer Engineering at the Politecnico di Torino (http://www.hpc.polito.it).

Appendix A. Supplementary data

Supplementary data to this article can be found online at https://doi.org/10.1016/j.fuel.2026.138455.

Data availability

The data that has been used is confidential.

References

[1] E. Toulson, H. J. Schock, and W. P. Attard, "A Review of Pre-Chamber Initiated Jet Ignition Combustion Systems," Oct. 2010. doi: 10.4271/2010-01-2263.
[2] Alvarez CEC, Couto GE, Roso VR, Thiriet AB, Valle RM. A review of prechamber ignition systems as lean combustion technology for SI engines. Elsevier Ltd.; 2018. 10.1016/j.applthermaleng.2017.08.118.
[3] Zhu S, Akehurst S, Lewis A, Yuan H. "A review of the pre-chamber ignition system applied on future low-carbon spark ignition engines". Elsevier Ltd; 2022. 10.1016/j.rser.2021.111872.
[4] Biswas S, Tanvir S, Wang H, Qiao L. On ignition mechanisms of premixed CH4/air and H2/air using a hot turbulent jet generated by pre-chamber combustion. Appl Therm Eng 2016;106:925–37. https://doi.org/10.1016/j.applthermaleng.2016.06.070.
[5] Biswas S, Qiao L. Prechamber hot jet ignition of ultra-lean h2/air mixtures: effect of supersonic jets and combustion instability. SAE Int J Engines 2016;9(3):1584–92. https://doi.org/10.4271/2016-01-0795.
[6] Gholamisheeri M, Thelen BC, Gentz GR, Wichman IS, Toulson E. Rapid compression machine study of a premixed, variable inlet density and flow rate, confined turbulent jet. Combust Flame 2016;169:321–32. https://doi.org/10.1016/j.combustflame.2016.05.001.
[7] Rajasegar R, Niki Y, García-Oliver JM, Li Z, Musculus MPB. Fundamental insights on ignition and combustion of natural gas in an active fueled pre-chamber spark-ignition system. Combust Flame 2021;232. https://doi.org/10.1016/j.combustflame.2021.111561.
[8] Pielecha I, Szwajca F, Skobiej K, Pielecha J, Merkisz J, Cieślik W. Analysis on monofuel: methane and hydrogen in passive TJI engine using Center of Combustion and lambda-value control. Int J Hydrogen Energy 2024;83:1170–83. https://doi.org/10.1016/j.ijhydene.2024.08.159.
[9] Jin Y, et al. Ignition timing effect on the combustion performance of hydrogen addition in methane fermentation gas in a local energy system. Fuel 2022;324. https://doi.org/10.1016/j.fuel.2022.124714.
[10] Soltic P, Hilfiker T. Efficiency and raw emission benefits from hydrogen addition to methane in a Prechamber–Equipped engine. Int J Hydrogen Energy 2020;45(43):23638–52. https://doi.org/10.1016/j.ijhydene.2020.06.123.
[11] Jeelan Basha KB, Balasubramani S, Sivasankaralingam V. "An experimental study on the influence of nozzle hole numbers and patterns of a passive pre-chamber spark ignition system". *Int J Hydrogen Energy* 2024;91:1207–20. https://doi.org/10.1016/j.ijhydene.2024.10.226.
[12] Lin Z, Liu S, Sun Q, Qi Y, Wang Z. Numerical investigation of multiple hydrogen injection in a jet ignition ammonia-hydrogen engine. Int J Hydrogen Energy 2024;77:336–46. https://doi.org/10.1016/j.ijhydene.2024.06.098.
[13] Zhu J, et al. Computational insights into flame development and emission formation in an ammonia engine with hydrogen-assisted pre-chamber turbulent jet ignition. Energy Convers Manag 2024;314. https://doi.org/10.1016/j.enconman.2024.118706.
[14] de Oliveira WP, Mendonça MS, Chavda NB, Rodrigues Filho FA, Baeta JGC. Numerical and experimental analysis of the combustion in a Single-Cylinder research engine with passive TJI pre-chamber operating with hydrated ethanol.

Energy Convers Manag 2024;310. https://doi.org/10.1016/j.enconman.2024.118459.
[15] Qiang Y, et al. Effect of injection strategy on the hydrogen mixture distribution and combustion of the hydrogen-fueled engine with passive pre-chamber ignition under lean burn condition. Fuel 2024;375. https://doi.org/10.1016/j.fuel.2024.132610.
[16] Qiang Y, et al. Study on the effect of variable valve timing and spark timing on the performance of the hydrogen-fueled engine with passive pre-chamber ignition under partial load conditions. Energy Convers Manag 2024;302. https://doi.org/10.1016/j.enconman.2024.118104.
[17] Maas R, Bekdemir C, Somers B. "Numerical study on the design of a passive pre-chamber for a heavy-duty hydrogen combustion engine". SAE Technical Papers SAE International. 2024. 10.4271/2024-01-2112.
[18] Gholamisheeri M, Wichman IS, Toulson E. A study of the turbulent jet flow field in a methane fueled turbulent jet ignition (TJI) system. Combust Flame 2017;183:194–206. https://doi.org/10.1016/j.combustflame.2017.05.008.
[19] Kim J, Scarcelli R, Som S, Shah A, Biruduganti MS, Longman DE. Assessment of turbulent combustion models for simulating prechamber ignition in a natural gas engine. J Eng Gas Turbine Power 2021;143(9):Sep. https://doi.org/10.1115/1.4050482.
[20] Ravindran AC, Kokjohn SL. The challenges of using detailed chemistry model for simulating direct injection spark ignition engine combustion during cold-start. Int J Engine Res 2023;24(1):161–77. https://doi.org/10.1177/14680874211045968.
[21] Posch S, Gößnitzer C, Lang M, Novella R, Steiner H, Wimmer A. "Turbulent combustion modeling for internal combustion engine CFD: a review". Elsevier Ltd; 2025. 10.1016/j.pecs.2024.101200.
[22] T. Poinsot and D. Veynante, "Theoretical and Numerical Combustion Second Edition.".
[23] Piano A, et al. CFD-based methodology for the characterization of the combustion process of a passive pre-chamber gasoline engine. Transp Eng 2023;13. https://doi.org/10.1016/j.treng.2023.100200.
[24] Feyz ME, Hasti VR, Gore JP, Chowdhury A, Nalim MR. Scalar predictors of premixed gas ignition by a suddenly-starting hot jet. Int J Hydrogen Energy 2019;44(42):23793–806. https://doi.org/10.1016/j.ijhydene.2019.07.066.
[25] Allison PM, de Oliveira M, Giusti A, Mastorakos E. Pre-chamber ignition mechanism: experiments and simulations on turbulent jet flame structure. Fuel 2018;230:274–81. https://doi.org/10.1016/j.fuel.2018.05.005.
[26] Benekos S, Frouzakis CE, Giannakopoulos GK, Altantzis C, Boulouchos K. A 2-D DNS study of the effects of nozzle geometry, ignition kernel placement and initial turbulence on prechamber ignition. Combust Flame 2021;225:272–90. https://doi.org/10.1016/j.combustflame.2020.10.045.
[27] Benajes J, et al. Computational assessment towards understanding the energy conversion and combustion process of lean mixtures in passive pre-chamber ignited engines. Appl Therm Eng 2020;178. https://doi.org/10.1016/j.applthermaleng.2020.115501.
[28] Malé Q, Staffelbach G, Vermorel O, Misdariis A, Ravet F, Poinsot T. Large eddy simulation of pre-chamber ignition in an internal combustion engine. Flow Turbul Combust 2019;103(2):465–83. https://doi.org/10.1007/s10494-019-00026-y.
[29] Han Z, Reitz RD. Turbulence modeling of internal combustion engines using RNG k-ε models. Combust Sci Technol 1995;106(4–6):267–95. https://doi.org/10.1080/00102209508907782.
[30] Colin O, Benkenida A, Angelberger C. 3D modeling of mixing, ignition and combustion phenomena in highly stratified gasoline engines. Oil and Gas Science and Technology 2003;58(1):47–62. https://doi.org/10.2516/ogst:2003004.
[31] O. Colin and A. Benkenida, "The 3-Zones Extended Coherent Flame Model (ECFM3Z) for Computing Premixed/Diffusion Combustion," 2004.
[32] Yang X, Solomon A, Kuo TW. "Ignition and combustion simulations of spray-guided SIDI engine using Arrhenius combustion with spark-energy deposition model". SAE Technical Papers SAE International 2012. https://doi.org/10.4271/2012-01-0147.
[33] Baratta M, Chiriches S, Goel P, Misul D. CFD modelling of natural gas combustion in IC engines under different EGR dilution and H2-doping conditions. Transp Eng 2020;2. https://doi.org/10.1016/j.treng.2020.100018.
[34] "Gregory P. Smith, David M. Golden, Michael Frenklach, Nigel W. Moriarty, Boris Eiteneer, Mikhail Goldenberg, C. Thomas Bowman, Ronald K. Hanson, Soonho Song, William C. Gardiner, Jr., Vitali V. Lissianski, and Zhiwei Qin http://www.me.berkeley.edu/gri_mech/.".
[35] Dong S, et al. A new detailed kinetic model for surrogate fuels: C3MechV3.3. Appl Energy Combust Sci 2022;9. https://doi.org/10.1016/j.jaecs.2021.100043.
[36] P. K. Senecal *et al.*, "Multi-Dimensional Modeling of Direct-Injection Diesel Spray Liquid Length and Flam Lift-off Length using CFD an Parallel Detailed Chemistry," 2003.
[37] C. Meneveau and T. Poinsot, "Stretching and Quenching of Flamelets in Premixed Turbulent Combustion," 1991.
[38] F. Charlette, C. Meneveau, and D. Veynante, "A Power-Law Flame Wrinkling Model for LES of Premixed Turbulent Combustion Part I: Non-Dynamic Formulation and Initial Tests," 2002.
[39] Bougrine S, Richard S, Colin O, Veynante D. Fuel composition effects on flame stretch in turbulent premixed combustion: Numerical analysis of flame-vortex interaction and formulation of a new efficiency function. Flow Turbul Combust 2014;93(2):251–89. https://doi.org/10.1007/s10494-014-9546-4.
[40] Suillaud E, Truffin K, Colin O, Veynante D. Direct Numerical Simulations of high Karlovitz number premixed flames for the analysis and modeling of the displacement speed. Combust Flame 2022;236. https://doi.org/10.1016/j.combustflame.2021.111770.
[41] R. Sola, M. Baratta, D. Misul, M. D'Elia, L. Ferretti, and J. K. Venkataramanan, "Premixed Hydrogen-Methane Combustion Modelling in a Pre-Chamber RCEM with Flamelet-Based and Detailed-Chemistry Approaches," Sep. 2025. doi: 10.4271/2025-24-0046.
[42] Colin O, Truffin K. A spark ignition model for large eddy simulation based on an FSD transport equation (ISSIM-LES). Proc Combust Inst 2011;33(2):3097–104. https://doi.org/10.1016/j.proci.2010.07.023.